University of New Orleans

ScholarWorks@UNO

University of New Orleans Theses and Dissertations

Dissertations and Theses

Summer 8-6-2018

Hydrodynamics of an Anguilliform Swimming Motion using Morison's Equation

Naga Sasi Devarakonda
ndevarak@uno.edu

Follow this and additional works at: https://scholarworks.uno.edu/td

 Part of the Ocean Engineering Commons

Recommended Citation

Devarakonda, Naga Sasi, "Hydrodynamics of an Anguilliform Swimming Motion using Morison's Equation" (2018). *University of New Orleans Theses and Dissertations*. 2524.
https://scholarworks.uno.edu/td/2524

This Thesis is protected by copyright and/or related rights. It has been brought to you by ScholarWorks@UNO with permission from the rights-holder(s). You are free to use this Thesis in any way that is permitted by the copyright and related rights legislation that applies to your use. For other uses you need to obtain permission from the rights-holder(s) directly, unless additional rights are indicated by a Creative Commons license in the record and/or on the work itself.

This Thesis has been accepted for inclusion in University of New Orleans Theses and Dissertations by an authorized administrator of ScholarWorks@UNO. For more information, please contact scholarworks@uno.edu.

University of New Orleans
ScholarWorks@UNO

University of New Orleans Theses and Dissertations | Dissertations and Theses

Summer 07-25-2018

Hydrodynamics of an Anguilliform Swimming Motion using Morison's Equation

Devarakonda Naga Sasi
University of New Orleans, ndevarak@uno.edu

Follow this and additional works at: http://scholarworks.uno.edu/td

 Part of the Other Engineering Commons

Recommended Citation
Devarakonda, Naga Sasi, "Hydrodynamics of an Anguilliform Body using Morisons Equation" (2018). *University of New Orleans Theses and Dissertations*. 3631.
http://scholarworks.uno.edu/td/3631

This Thesis is brought to you for free and open access by the Dissertations and Theses at ScholarWorks@UNO. It has been accepted for inclusion in University of New Orleans Theses and Dissertations by an authorized administrator of ScholarWorks@UNO. The author is solely responsible for ensuring compliance with copyright. For more information, please contact scholarworks@uno.edu.

Hydrodynamics of an Anguilliform Swimming Motion using Morison's Equation

A Thesis

Submitted to the graduate faculty of the
University of New Orleans
In partial fulfillment of the
requirements of the degree

Master of Science
in
Engineering
Naval Architecture and Marine Engineering

by

Naga Sasi Devarakonda

B. Tech, Andhra University Visakhapatnam, 2016

August 2018

ACKNOWLEDGEMENT

I am grateful to Kelly Cooper, Program Manager, Office of Naval research, for awarding funding to the department and experimental analysis of the robotic eel presented within. This funding was awarded through a grant number N00014-11-1-0830 to Dr. Brandon Taravella at School of Naval Architecture and Marine Engineering, UNO. If it hadn't been, none of this would have been accomplished.

I would like to thank Dr. Brandon M. Taravella for his support in this thesis process, and he made sure I was on the right track. He supported by efficiently suggesting those additions that would never have occurred to me. His extensive support made it easier for me to complete my thesis. His timely response through emails and meetings never let me feel any stress. He is my primary resource for getting my questions answered and was instrumental in helping me crank out this thesis, all within time. Thank you so much for your time and attention.

I would also like to thank my family for giving me all the support, understanding and for showing lots of patience for me. My sister has been my best friend all my life, and I love her dearly and thank her for all her advice and support. I know I always have my family to count on when times are rough. I also thank my uncle and aunt for all their support throughout.

I appreciate my friends for supporting me during the tight schedule and helping me finish my thesis.

- Naga Sasi. D

Table of Contents

List of Figures

List of Tables

ABSTRACT

In this study, the hydrodynamic performance of anguilliform swimming motion is computed using Morison's equation. This method was shown to predict the servo motor torques well. The anguilliform swimming motion is sinusoidal with increasing amplitude from head to tail. A "wakeless" swimming motion proposed by Vorus and Taravella (2011) with zero net circulation is considered.

This method is compared to the existing slender body theory and is validated with reference to the experimental results of NEELBOT-1.1 (Potts, 2015). The results for the study indicates that self-propulsion speed of the motion is independent of the oscillating tail amplitude at a constant advance ratio. At a constant wave speed, the self-propulsion speed attains a local maximum at an advance ratio of 0.5. Where the nominal length is equal to half the wavelength.

Keywords: Hydrodynamics, Anguilliform motion, Morison's Equation

1. Introduction

The extension of robots and other automated technology is seen in various fields – military, manufacturing, medicine, domestic uses, research and development, etc. This study is mainly focused on an anguilliform robot. Anguilliform swimmers (eels, lamprey, etc.) are flexible throughout and flexing approximately one-half wavelength. They are observed to travel with greater speeds in comparison to their muscle power.

Underwater vehicles are of interest in different fields like military, environmental survey, scientific research of the world's oceans. In naval warfare (ISR and SAR missions) these robots can be used in surveillance of coarse shallow water. Sometimes, surveillance and data collection are needed in dangerous situations where personnel cannot be put at risk. To reduce this risk, new methods and technologies are introduced involving Autonomous Underwater Vehicles (AUV's) which are efficient, flexible, noiseless, radar resistant and stealthy to carry vigilance devices into hazardous areas.

Secondly, the anguilliform robot can be used in ocean research for testing salinity, acidity, density and other environmental properties. These can also be used in discovering new underwater species by attaching cameras and data collection devices to the robot. This technology can be applied in monitoring in unmanned or inaccessible places like underground toxic sewage tanks, pipes, deep sea units, as well as human intestine and circulatory system in a microscopic level.

Finally, the most crucial importance as per this study is the academic one. Researchers are trying to bring the theoretical and experimental aspects of the robot closer by studying its propulsive wake. Theoretically, the motion of the robot is being computed using the three-dimensional anguilliform motion proposed by Vorus and Taravella (2011). The hydrodynamic performance is predicted using Morison's equation. Experimentally, the robot was tested in a towing tank and the forces along with the wake were measured using load cell and PIV testing (Potts, 2015).

Morison's equation was developed to describe the wave forces acting on cylindrical structures in the offshore industry (Chakrabarti, 1985). It is a semi-empirical equation composed of two components, inertia force and drag force. Morison's equation is applicable when drag force is significant. This method is predominant in case of symmetric oscillating objects with high Reynolds number, where force may be obtained in a closed form. The force coefficients are determined based on Keulegan-Carpenter parameter (KC).

1.1. Literature Survey

Fish propulsion has been studied for many years. Pettigrew (1873) observed the shape of propulsive wave of fish, Houssay (1912) attempted to measure thrust and drag of fish. The different types of propulsive movements in fish are classified by Breder (1926). Gray (1936) used hydrodynamic theory of drag for rigid bodies of revolution and compared this with the then best-known values for mammalian muscle power output. He suggested that dolphins swim many times faster than their muscle power allows them. He was also the first, to quantitatively demonstrate that the eel's body undulations have the form of backward travelling wave. Taylor (1952) used hydrofoil theory to formulate a quantitative hydrodynamic model for fish propulsion. He also evaluated the speed at which the eel propels itself at the least energy output.

Lighthill (1952) researched on hydromechanics with small animals (flagella, amoeba) at low Reynolds number where viscosity dominates. Ideal flow theory with vortex shedding is implemented on this motion accounting simple skin friction with corrections in Lighthill (1960). Animals such as lamprey with higher Reynolds number, where thin boundary layer flows prevail are studied in Lighthill (1971).

In recent years, several efforts are made to decrease the span between the biological eels and the mechanical robots. Vorus (2005) developed a two-dimensional solution using ideal flow theory for the displacement waveform which develops zero circulation around the body length over time. He also

implied that, for a real fluid, similar bodies with a thin boundary layer and same deformation mode shape, self-propel without vortex shedding, rotational wake, and induced drag. The anguilliform swimming differs from the carangiform and tunniform swimming as it produces higher thrust from the global body motions.

The theory of 3-D anguilliform motion in Vorus and Taravella (2011) is based on a 2-D anguilliform motion in Vorus (2005). They utilized slender body theory to develop an anguilliform motion that would develop thrust without producing an induced drag.

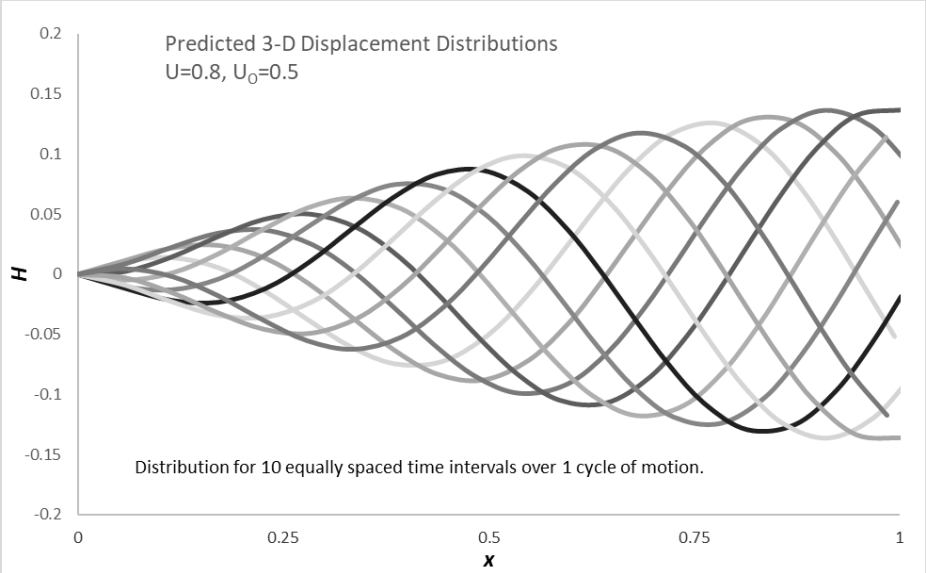

Fig. 1 Displacement distribution by 3-D anguilliform swimming motion theory

Later, Potts (2015) developed an anguilliform robot model which attempted to replicate the 3-D anguilliform displacement theory. He measured velocity vectors using Stereoscopic Particle Image Velocimetry (SPIV) equipment. He compared these experimental results (thrust and flow-field velocity) to the values computed using 3-D theory by Vorus and Taravella (2011). He proved that the quasi-steady method of predicting drag (i.e., ITTC friction line) was not adequate to predict the propulsion characteristics of an anguilliform swimming motion by comparing the theoretical results of ideal motion

to the experimentally produced off-design results. He also proved that the 3-D anguilliform swimming motion equation (1) well predicts the kinematics of the anguilliform swimming robot.

Apneseth, Day and Clelland (2009) have built, developed and tested a three-segment model and compared its hydrodynamic performance to the predictions from a Morison based approach. Three main series of tests were carried out with the model in the towing tank. These tests are determined as single flapper (zero forward speed and the two segments act as rigidly joined), double flapper (zero forward speed and larger amplitudes in the aft segments) and final set included range of speeds to determine the self-propulsion point. They determined that the mean thrust at zero speed and self-propulsion speed increase quadratically. This approach was proved to predict the self- propulsion speed with high accuracy.

1.2. Current Study

In the present study, the compatibility of Morison's equation with the anguilliform swimming motion is investigated. The validity of this approach is checked by comparing the results to the values obtained by the slender body theory outlined in Vorus and Taravella (2011) and experimental work of Potts (2015). This work is focused on examining the adaptability of Morison's equation to multi-segmented eel-like structure.

The hydrodynamic qualities of the robot are computed at constant flow velocity and advance ratio. The basic steps involved in the computational analysis are:

1. Computing the nominal length
2. Non-dimensionalizing with respect to nominal length and wave speed
3. Computing the joint locations and the mid-points of the sections using cylindrical coordinate system
4. Computing body velocities and accelerations from the predefined displacement (Vorus and Taravella, 2011)

5. Computing longitudinal and transverse hydrodynamic forces at midpoints of the segments using Morison's equation
6. Computing forces and torque at every servo joint
7. Post-processing and analysis of the results for the forward speed

In this study, the transverse flow field velocities and accelerations of the twenty-segmented model are computed using the motion prescribed in Vorus and Taravella (2011). Morison's equation is implemented for computing thrust. These results are compared to off-design experimental results from Potts (2015) and his computations using force equations from slender body theory.

The self-propulsion speed is predicted by varying the parameters that affect the longitudinal force. The parameters are the advance ratio (U), flow speed (U_O) and the oscillating body amplitude (Γ).

2. Background

2.1. Three-dimensional Ideal Anguilliform Swimming Motion

The three-dimensional ideal anguilliform swimming motion has proven to be highly efficient theoretically in Vorus and Taravella (2011). The anguilliform swimming motion was described in Vorus and Taravella (2011) using the combination of ideal flow theory and slender body theory. In this derivation, the flow is found to be wakeless with zero vorticity, essentially removing the induced drag. Conditions of no shedding and continuously zero circulation over the body is considered. This theory uses doublets constrained to the *x*-axis to determine the physical shape of the eel in the flow.

A brief description of the 3-D ideal anguilliform swimming motion given in Vorus and Taravella (2011) is discussed in the following. The analysis assumes high Reynolds number and a thin boundary layer, which allows for the use of ideal-flow theory.

Vorus and Taravella (2011) developed an equation for an ideal anguilliform swimming motion, which is said to produce zero drag as

$$\bar{h}(\bar{x},\bar{t}) = \Gamma\left[\sin\left(2\pi\left(\frac{\bar{x}}{U}-\bar{t}\right)\right)-\sin\left(2\pi(\bar{x}-\bar{t})\right)\right] \tag{1}$$

Where, the displacement amplitude (Γ) is a function of desired thrust and cross-sectional radius. The advance ratio (*U)* which can be defined as the ratio of the body velocity (U_o) and the wave velocity (*V*), since the slip is assumed to be zero. $\bar{x}$ and $\bar{t}$ are the non-dimensionalized position along horizontal *x*-axis and time respectively. To elaborate, the normalized transverse displacement (*h*), longitudinal displacement position (*x*) and time (*t*) are shown below

$$\bar{h}(\bar{x},\bar{t}) = \frac{h(x,t)}{L} \qquad \bar{x} = \frac{x}{L} \qquad \bar{t} = \frac{Vt}{L} \tag{2}$$

The sectional forces per unit length in the *x* and *y* directions are derived in Vorus and Taravella (2011) using Bernoulli equation to be

$$f_y(x,t) = -\rho\pi r_o^2 k(x,t) \tag{3}$$

$$f_x(x,t) = \rho\pi r_o^2 k(x,t) h_x(x,t) = -f_y(x,t) h_x(x,t) \tag{4}$$

Where $k(x,t)$ is defined as

$$k(x,t) = h_{tt} + 2U_o h_{xt} + U_o^2 h_{xx} \tag{5}$$

U_o is the advanced flow speed.

The arc length of the articulating displacement wave extends and contracts. To maintain a constant value, a theoretical length *L* is imposed in our calculations. In Potts (2015), it is computed as a time average of the longitudinal straight-line distance from head to a line both perpendicular to the horizontal axis and intersecting the tail of the articulating eel for the cycle of motion as shown in Fig. 2. The nominal length (*L)* is computed by the equation:

$$L = \frac{1}{N}\sum_{n=0}^{N} L_n \tag{6}$$

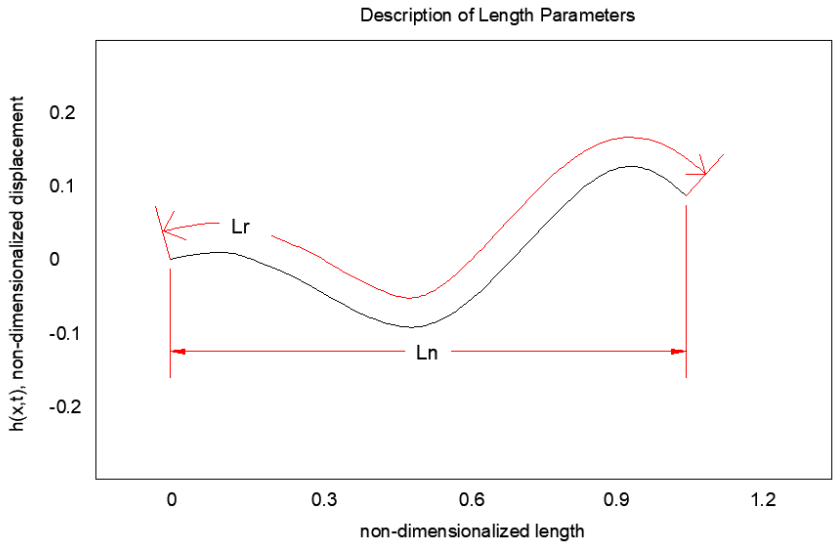

Fig. 2 Annotations denoting the length parameters of the anguilliform shape for one-time step of the motion.

Where, *N* is the number of time steps, computed by

$$N = \frac{T}{dt} \tag{7}$$

T is the time period at which the eel operates and is given as $T = \frac{1}{f} = \frac{L}{V}$.

2.2. Morison's Equation

Morison's equation was developed by Morison, O'Brien, Johnson, and Schaaf (1950). It calculates the wave forces on offshore structures. It is a semi-empirical equation for inline forces on a body in an oscillatory flow. In this study, hydrodynamic forces taken at the midpoints of the segment ($F_{Hx,n}$ and $F_{Hy,n}$) are calculated using Morison's equation on inclined cylinders (Chakrabarti, 1987).

Morison's equation is composed of inertia and drag components linearly added together. It is applicable where drag forces are significant. It is an appropriate method for computing forces when the size of the submerged body D/L < 0.2 and the Reynolds number is high. The assumptions involved in this method are:

1. Section does not affect the neighboring sections.
2. The body does not pierce the free surface.

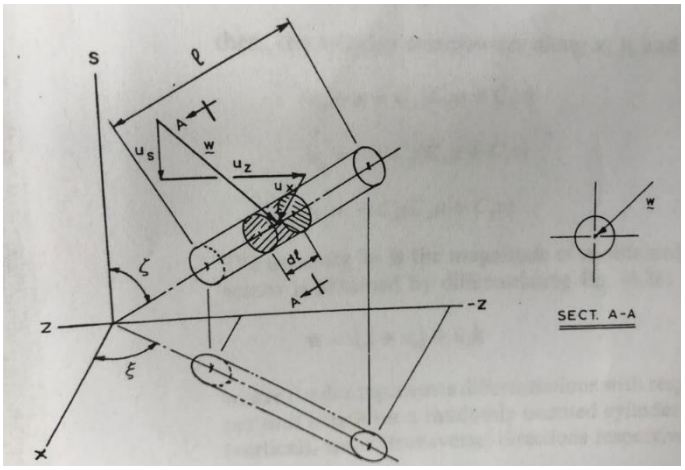

Fig. 3 Definition sketch of Morison equation application on an inclined cylinder (Source: S.K. Chakrabarti, Hydrodynamics of Offshore Structures, Fig. 6.4)

An extension of Morison's equation to an inclined cylinder is derived in S. K. Chakrabarti (1987). A description of this method is elaborated in the following using Fig. 3. The normal force to the cylinders is given as

$$\bar{\boldsymbol{f}} = C_M A_I \dot{\bar{\boldsymbol{w}}} + C_D A_D |\bar{\boldsymbol{w}}| \bar{\boldsymbol{w}} \tag{8}$$

Where, $\bar{w}$ and $\dot{\bar{w}}$ are the normal velocity and the acceleration of the flow over an inclined cylinder. The velocity normal to the cylinder is written as

$$\bar{\boldsymbol{w}} = \boldsymbol{C}(u\bar{\boldsymbol{\imath}} + v\bar{\boldsymbol{\jmath}}) \times \boldsymbol{C} \tag{9}$$

$\boldsymbol{C}$ is the unit vector along the cylinder axis: $\boldsymbol{C} = C_x\bar{\boldsymbol{\imath}} + C_y\bar{\boldsymbol{\jmath}} + C_z\bar{\boldsymbol{k}}$ and *u*, *v*, *w* are the velocities in the direction of the three Cartesian axes.

Morison's equation is applied on every individual segment *i* in a time stepping manner. The forces are calculated for every segment using the flow velocity and acceleration at their mid-points of the *N* segments. In the spherical coordinate system,

$$C_{x,i} = \sin\zeta_i \cos\xi_i \qquad C_{y,i} = \cos\zeta_i \qquad C_{z,i} = \sin\zeta_i \sin\xi_i$$

Where, $\zeta_i$is the angle made by the segment with the y-axis and ξ_i is the angle made by the projection of the segment with the x-axis. (ξ_i is zero in our case as a 2-D motion is considered).

$\overline{w_i}$ and $\dot{\overline{w_i}}$ are the velocity and acceleration normal to the segment *i* and are written as

$$\overline{\boldsymbol{w_\imath}} = u_{x,i}\bar{\boldsymbol{\imath}} + u_{y,i}\bar{\boldsymbol{\jmath}} + u_{z,i}\bar{\boldsymbol{k}} \tag{10}$$

$$\dot{\overline{\boldsymbol{w}}}_{\boldsymbol{\imath}} = \dot{u}_{x,i}\bar{\boldsymbol{\imath}} + \dot{u}_{y,i}\bar{\boldsymbol{\jmath}} + \dot{u}_{z,i}\bar{\boldsymbol{k}} \tag{11}$$

The velocity components of segment *i* along *x*, *y* and *z* are given as

$$u_{x,i} = u - C_{x,i}\left(C_{x,i}u + C_{y,i}v_i\right) \tag{12}$$

$$u_{y,i} = v_i - C_{y,i}\left(C_{x,i}u + C_{y,i}v_i\right) \tag{13}$$

$$u_{z,i} = -C_{z,i}\left(C_{x,i}u + C_{y,i}v_i\right) \tag{14}$$

Where, u is the horizontal velocity on the earth-coordinate system and is equal to the free stream velocity (U_O) which is in the positive direction, i.e., from head to tail. *v* is the transverse velocity in the earth coordinate system and is given by $h_t(x,t)$ from the 3-D anguilliform motion of Vorus and Taravella (2011).

Thus, the forces per unit length calculated on each segment is given as,

$$f_{x,i} = C_M A_I \dot{u}_{x,i} + C_D A_D |\bar{\boldsymbol{w}}| u_{x,i} \tag{15}$$

$$f_{y,i} = C_M A_I \dot{u}_{y,i} + C_D A_D |\bar{\boldsymbol{w}}| u_{y,i} \tag{16}$$

$$f_{z,i} = C_M A_I \dot{u}_{z,i} + C_D A_D |\bar{\boldsymbol{w}}| u_{z,i} \tag{17}$$

Where, $\dot{u}_{x,i}$, $\dot{u}_{y,i}$ and $\dot{u}_{z,i}$ accelerations obtained by derivation of equations (12, 13, 14) with respect to time respectively. The constants A_I and A_D of equations 15 through 17 are given as

$$A_I = \pi\rho {r_o}^2$$

$$A_D = \rho r_o$$

Where r_O is the cross-sectional radius and ρ is the mass density of the fluid. The added mass coefficient (C_M) and the drag coefficient (C_D) are based on the Keulegan Carpenter Number (*KC*).

The first term is the component of the inertial force and the latter is the resolved Morison drag force. The hydrodynamic forces acting on the cylinder along the segment length (l_n) acting on the midpoints is given as:

$$F_{Hx,i} = l_i f_{x,i} \tag{18}$$

$$F_{Hy,i} = l_i f_{y,i} \tag{19}$$

$i\epsilon[1, N]$, where *N* is the number of segments.

The instantaneous thrust is the sum of longitudinal forces of all the segments. The thrust force at time step *t* is calculated as

$$T(t) = \sum_{i=1}^{N} F_{Hx,i}(x, t) \tag{20}$$

The mean thrust can be obtained by integrating this over a whole cycle of motion and dividing by the number of time steps.

3. Numerical Development of NEELBOT-1.1

3.1. NEELBOT-1.1

NEELBOT-1.1 shown in Fig. 4 is a 20-segmented robot with 19 servo-actuators. It has an overall length of 1.35m (The span is taken excluding the hemispheric domes. Hence, a length of 1.3m is used for analysis.) and each segment is measured to be 65mm. It has a latex waterproofing skin and the overall diameter is 55mm.

Fig. 4 NEELBOT-1.1 with the latex rubber skin. (Source: Potts (2015), Figure 3.2.1.3)

Each segment is equipped with a Dongbu Herkulex DRS-0201 Servo-actuator. They are closed-loop PID position controllers with programmable PID gains. The specifications of these servo motors are shown in Table 1. Two AAA batteries are placed in each segment to provide power to the actuators and wireless communications. This equipment is shown in Fig. 5.

Table 1 Dongbu Herkulex DRS-0201 physical characteristics and specifications.

Parameter	Value
Width	45 mm
Depth	24 mm
Height	31 mm
Mass	60 g
Gear ratio	1:266
Voltage	7-12 VDC
Current	670 mA @ 7.4 V
Stall torque	2.4 N-m
Max speed	408 deg/sec

Table 2 lists parametric values of the robot used in this study for further analysis. The nominal length of the robot is obtained by converging it though iterations as shown in equation (6). In the following analysis, all of the terms are non-dimensionalized by nominal length (L) and the wave velocity (V).

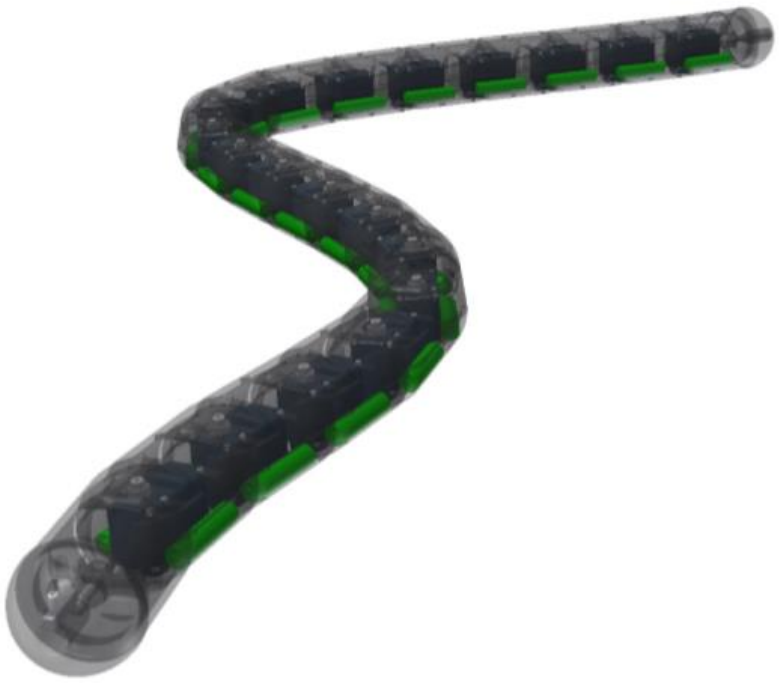

Fig. 5 Rendering of NEELBOT-1.1 showing off its sleek curves. The green cylinders are the AAA batteries with 2 per segment, and the dark blue boxes are the servo-actuators. (Source: Potts (2015), Figure 3.11)

Table 2 Parametric Values of the robot

Parameter	Value
Advanced speed, U_o	0.25 m/s
Advance ratio, U	0.7
Disp. Wave speed, $V = U_o/U$	0.357 m/s
Robot length, L_r	1.3 m
Nominal length, L	1.01 m
Radius	0.05 m
Time period, T	2.829 s
Amplitude, Γ	0.11767 (non-dimensional)
Number of segments	20

3.2. Kinematic Development

Vorus and Taravella (2011) state that animals such as an eel have higher Reynolds number and a thin boundary layer. The model maintains a high Reynolds number around 32,000, so that the boundary layer remains attached. This implies 3-D anguilliform swimming theory developed by Vorus and Taravella (2011) based on ideal flow theory.

The model is discretized such that the nodes replicate the segment joints of the robot. One motion cycle is divided into twelve equally spaced time steps. The computation of joint locations during a time step is an iterative process. Fig. 6 shows the behavior of motion throughout the path cycle which is obtained by equation (1). The solid line represents the form of the body at the initial time step (t=0).

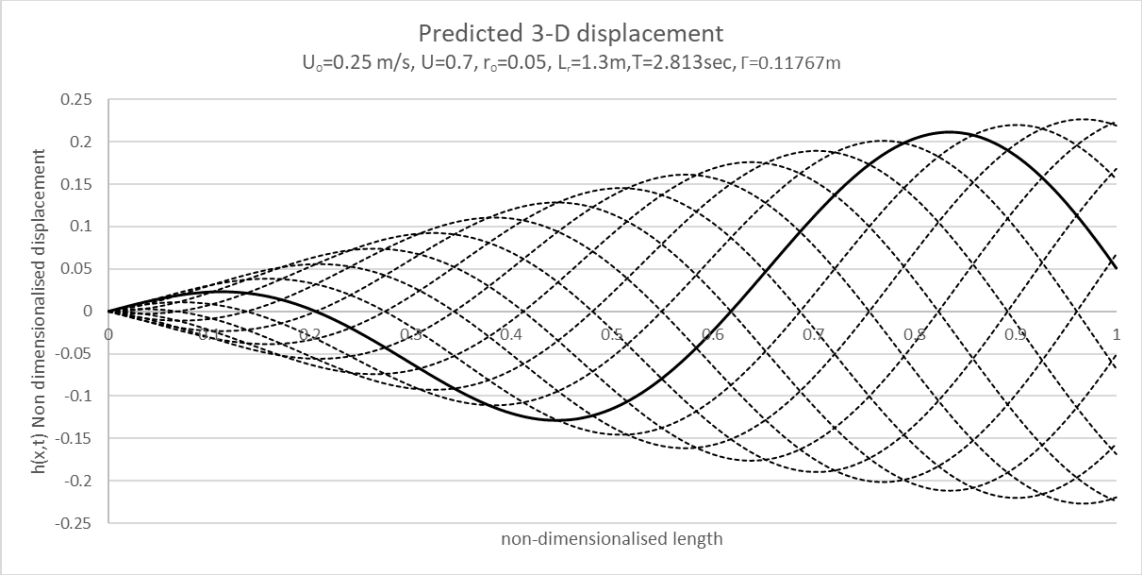

Fig. 6 Anguilliform motion plotted using 3-D displacement theory for 12 equally spaced time steps

3.2.1. Ideal Motion

In an ideal design motion shown in Fig. 7, the body produces forward thrust and the circulation around the body is hypothesized to be zero. The motions do not shed any vortices, thus implies zero induced drag.

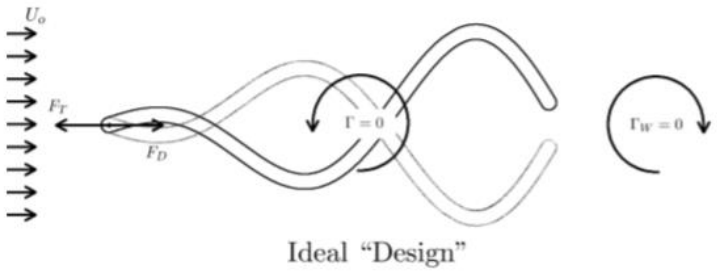

Fig. 7 Schematic showing dynamics of ideal design of the anguilliform robot motion (the lighter-colored outline contrasted with the darker-colored one denote the unsteady motion of the anguilliform shape). (Source: Potts (2015), Figure 5.3)

The joint locations of the segments at different time steps are obtained by converging the angle made by each of the segment with the *x*-axis (θ_i). The *x* and *y* coordinates of the joints are determined using the cylindrical coordinate system with respect to the head of the eel. Fig. 8 shows the actual behavior of the body along with the joint locations at different time steps throughout the path cycle for an ideal motion.

$$x_{t,i+1} = l_i \cos\theta_i + x_{t,i} \tag{21}$$

$$y_{t,i+1} = l_i \cos\theta_i + y_{t,i} \tag{22}$$

$i\epsilon[1, N]$, where *N* is the number of segments and *t* is the time step.

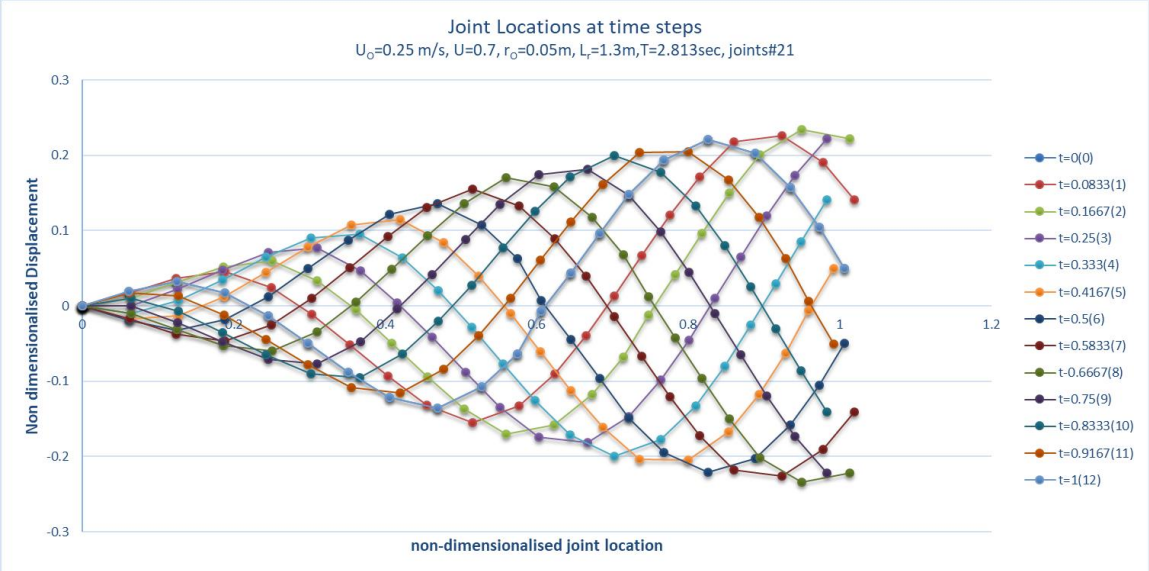

Fig. 8 Theoretically computed joint locations at different time steps for a motion cycle for an ideal motion. The points show the location of the servo joints.

3.2.2. Non-ideal motion

Potts (2015) found that the desired ideal motion was not replicated consistently by the robot during the SPIV testing. This was explained by the off-design cases shown in Fig. 9, which involves oscillating transverse lift force, a periodic forward thrust, induced drag, and shed circulation, or vortices, in the wake downstream from the motion.

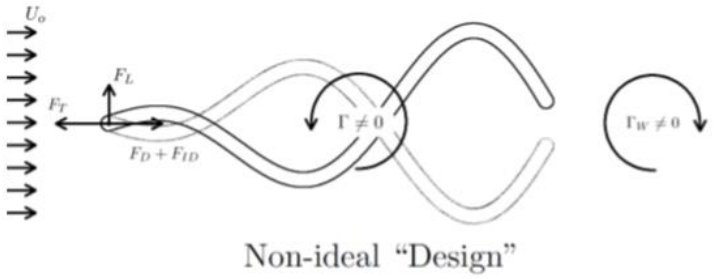

Fig. 9 Schematic showing dynamics of the non-ideal design of the anguilliform robot motion (the lighter-colored outline contrasted with the darker-colored one denote the unsteady motion of the anguilliform shape). (Source: Potts (2015), Figure 5.2)

A transfer function ($\bar{f}$) was introduced by Potts (2015) in the 3-D displacement anguilliform swimming theory developed for ideal shape by Vorus and Taravella (2011). This sinusoidal transfer function is multiplied to equation (1) to get the non-ideal shape. It is a sinusoidal function of the horizontal location.

$$\bar{f} = 1 + A \sin 2\pi F(\bar{x} + \tau) \tag{23}$$

Where, $\bar{x}$ is the non-dimensionalized horizontal location, *A* is 0.35, *F* is 0.14 and τ is -0.25.

$$\bar{h}(\bar{x}, \bar{t}) = \bar{f}\Gamma\left[\sin\left(2\pi\left(\frac{\bar{x}}{U} - \bar{t}\right)\right) - \sin\left(2\pi(\bar{x} - \bar{t})\right)\right] \tag{24}$$

Fig. 10 shows the non-ideal motion of the robot as computed from equation (24).

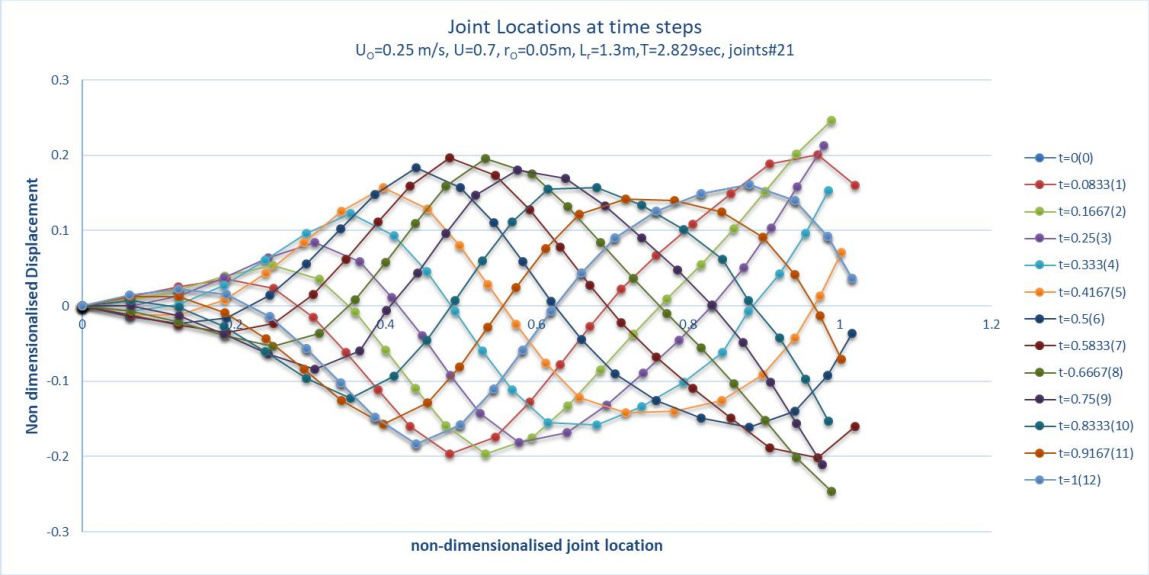

Fig. 10 Theoretically computed joint locations at different time steps for a motion cycle for a non-ideal motion. The points show the location of the servo joints.

However, after analyzing he stated that the velocities and accelerations can be well predicted using ideal flow theory.

3.2.3. Velocities and Accelerations

The kinematic quantities of velocity and acceleration are calculated at mid-points of each segment using equations developed from equation (1) with respect to time (*t*). Fig. 11 and Fig. 12 give the dimensionalized transverse velocities and accelerations respectively for every segment over time (*t*). The longitudinal flow velocity is U_O and longitudinal flow acceleration is zero. Below are the plots of velocities and acceleration with respect to the time steps for all the 20 segments of the robot for an ideal motion.

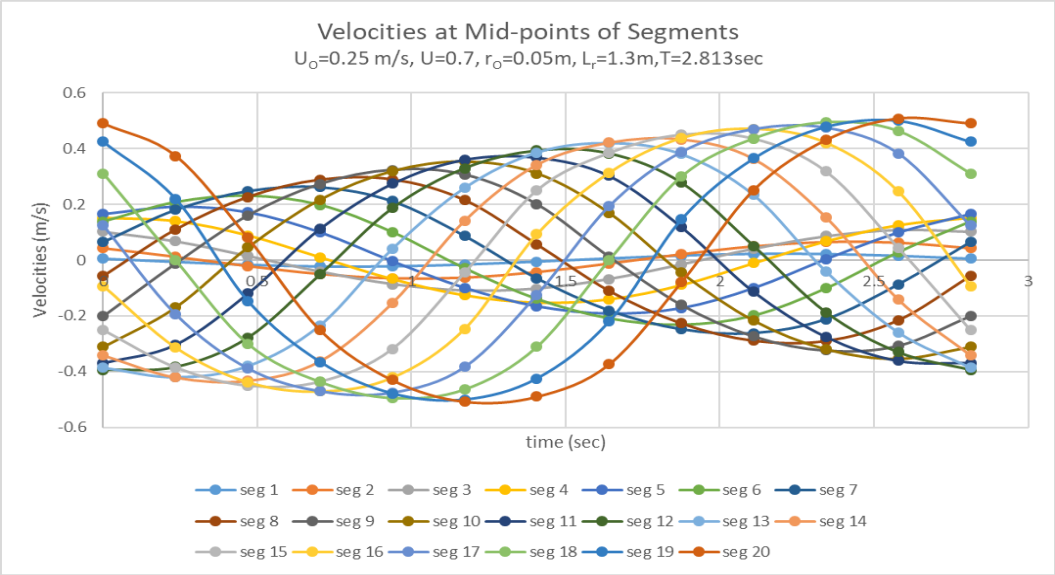

Fig. 11 Transverse velocities at the midpoints of the 20 segments plotted over time

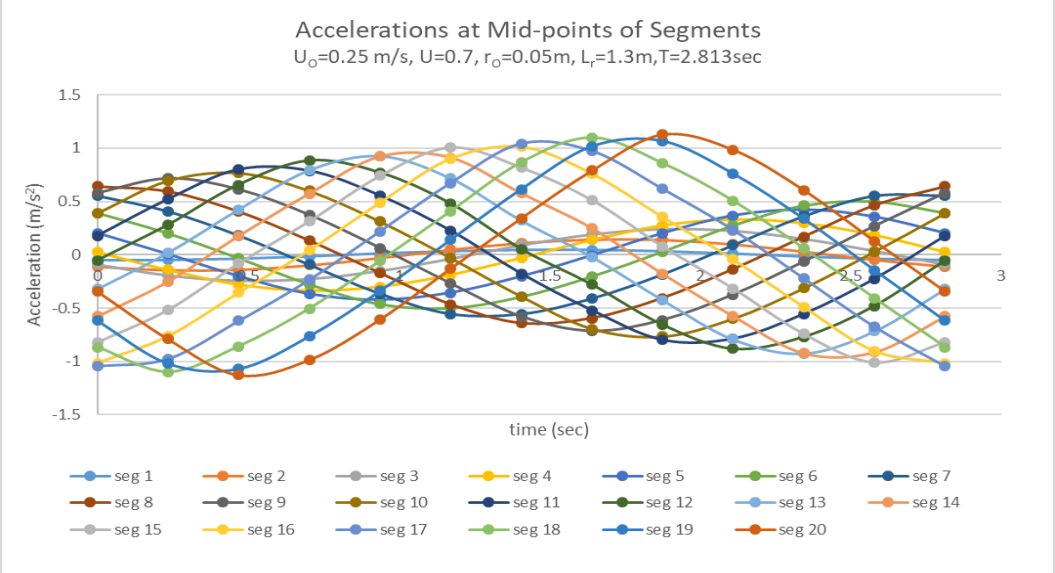

Fig. 12 Transverse accelerations at midpoints of the 20 segments plotted over time

3.3. Dynamic Development

In the following section, the dynamic development of the body is explained. Forces and moments (torques) are computed at every joint for all the time steps in a cycle of motion of the eel robot. These forces and moments are calculated by solving the equilibrium system of matrix equations.

The hydrodynamic forces for these bodies are computed using Morison's equation explained in section 2.2. Equation (18) and equation (19) give the longitudinal and transverse forces respectively.

These forces are calculated using the transverse velocities and accelerations obtained from the 3-D motion prescribed by Vorus and Taravella (2011). The behavior of total inertia and drag components for the various time steps along the path cycle, computed in the longitudinal direction is shown in Fig. 13.

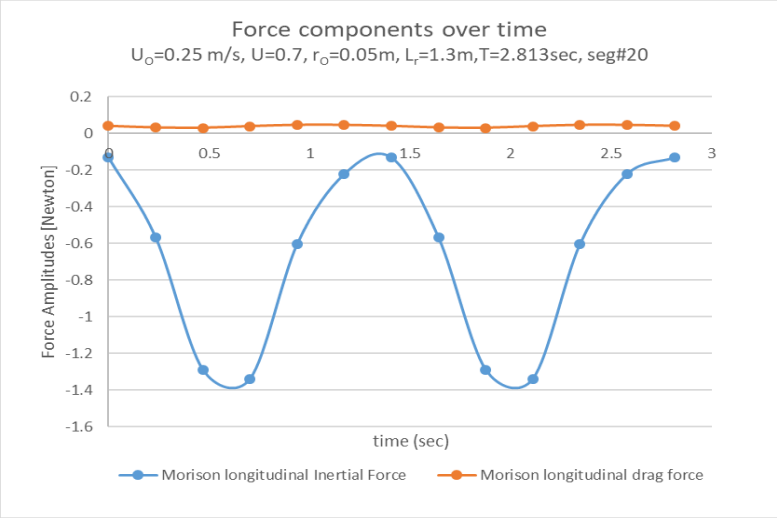

Fig. 13 Inertia and Drag components in the longitudinal direction computed using Morison's Equation are plotted over time

The behavior of longitudinal and transverse forces with respect to time for the 20 segments are shown in Fig. 14 and Fig. 15 respectively. The longitudinal force oscillates about zero along with the oscillation of the segment. The transverse force of each segment is directed towards the reference axis in the motion. The amplitude of the transverse force increases from head to tail.

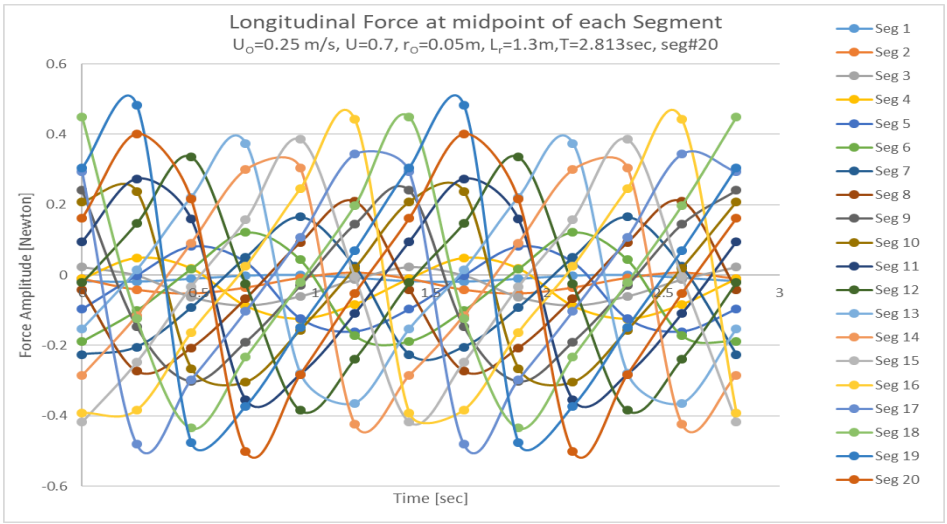

Fig. 14 Computed Longitudinal forces of the model over time using Morison's Equation

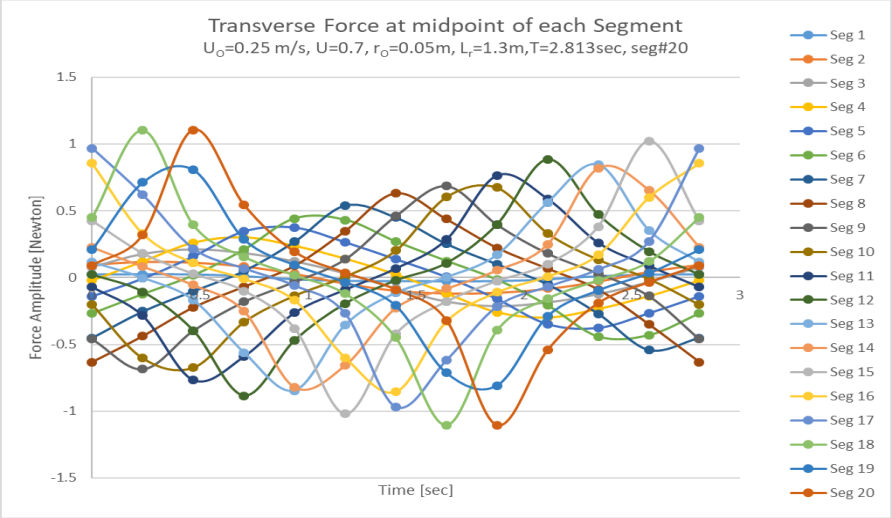

Fig. 15 Computed Transverse forces of the model over time using Morison's Equation

3.3.1. Untethered Swimming Case (free swimming)

The forces and moments can be obtained by solving the matrix equation (29) developed from the force equilibrium system of equations. Fig. 16 shows the free body diagram of a segment *n*.

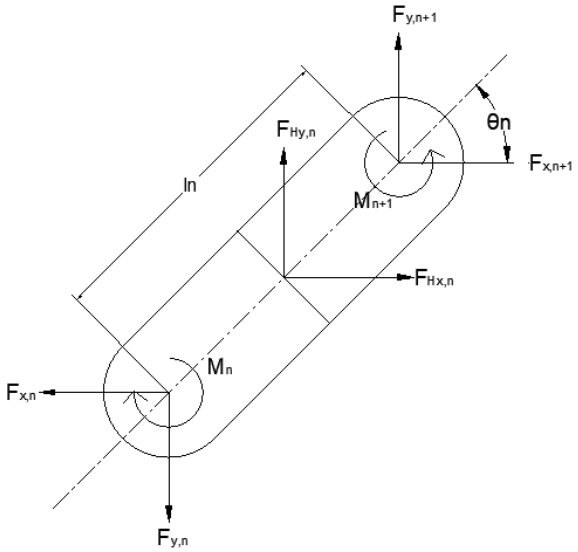

Fig. 16 Free- body diagram of a segment n.

The boundary conditions for the untethered motion are that the forces and moments at the first node (tip of head) and the last node (tail end) are zero.

$$F_{x,1} = 0 \qquad F_{x,N+1} = 0$$
$$F_{y,1} = 0 \qquad F_{y,N+1} = 0 \tag{25}$$
$$M_1 = 0 \qquad M_{N+1} = 0$$

Where *N* is the total number of segments.

From the free-body diagram, the equilibrium system of equations obtained from summation of forces (longitudinal and transverse) and moments can be written as,

$$\sum F_x = -F_{x,n} + F_{x,n+1} + F_{Hx,n} = m_n A_x \tag{26}$$

$$\sum F_x = -F_{y,n} + F_{y,n+1} + F_{Hy,n} = m_n(a_{n,y} + A_y + \alpha_E l_n(-\frac{N}{2} + n - 0.5)) \tag{27}$$

$$\sum M_z = -M_n + M_{n+1} + \left(F_{y,n+1} + F_{y,n}\right)\frac{l_n}{2}\cos\theta - (F_{x,n+1} + F_{x,n})\frac{l_n}{2}\sin\theta = I_n(\alpha_{z,n} + \alpha_E) \tag{28}$$

$n\epsilon[1, N]$

Solving equations (26), (27) and (28) and rearranging them in a matrix form, we get the equations of motion as

$$\boldsymbol{A}f = \boldsymbol{B} \tag{29}$$

Where,

$$A = \begin{bmatrix} -1 & 0 & 0 & 1 & 0 & 0 & \cdots & -m_n & 0 & 0 \\ 0 & -1 & 0 & 0 & 1 & 0 & \cdots & 0 & -m_n & -m_n(-\frac{N}{2} + n - 0.5) \\ -\frac{l_n}{2}\sin\theta & \frac{l_n}{2}\cos\theta & -1 & -\frac{l_n}{2}\sin\theta & \frac{l_n}{2}\cos\theta & 1 & \cdots & 0 & 0 & -I_n \\ \vdots & \vdots & \vdots & \vdots & \vdots & \vdots & \ddots & \vdots & \vdots & \vdots \\ -1 & 0 & 0 & 1 & 0 & 0 & \cdots & -m_N & 0 & 0 \\ 0 & -1 & 0 & 0 & 1 & 0 & \cdots & 0 & -m_N & -m_N(\frac{N}{2} - 0.5) \\ -\frac{l_N}{2}\sin\theta & \frac{l_N}{2}\cos\theta & -1 & -\frac{l_N}{2}\sin\theta & \frac{l_N}{2}\cos\theta & 1 & \cdots & 0 & 0 & -I_N \end{bmatrix}_{3N\times(3N+6)}$$

$$f = \begin{bmatrix} F_{x,n} \\ F_{y,n} \\ M_n \\ F_{x,n+1} \\ F_{y,n+1} \\ M_{n+1} \\ \vdots \\ A_x \\ A_y \\ \alpha_E \end{bmatrix}_{(3N+6)\times 1}$$

and

$$B = \begin{bmatrix} -F_{Hx,n} \\ m_n a_{n,y} - F_{Hy,n} \\ I_n \alpha_{z,n} \\ \vdots \\ -F_{Hx,N} \\ m_N a_{N,y} - F_{Hy,N} \\ I_N \alpha_{z,N} \end{bmatrix}_{3N\times 1}$$

Where, $a_{n,y}$ and $\alpha_{z,n}$ are the local accelerations of the segments at the mid-points obtained from 3D anguilliform swimming motion.

After applying the boundary conditions (Refer equation 25 and 30 in the respective cases) the inertia matrix *A* simplifies into a square matrix. The new dimensions of the matrices are:

$$A: [3N \times 3N]$$

$$f: [3N \times 1]$$

$$B: [3N \times 1]$$

Here, *f* is the matrix of unknowns which gives us the forces and moments at the joints.

There are 19 servo motors used in the model. The moment computed at each joint gives the maximum torque at each servo motor for a design speed of 0.25m/s in a tethered case. The servo torques for the tethered cases are plotted over time in Fig. 17.

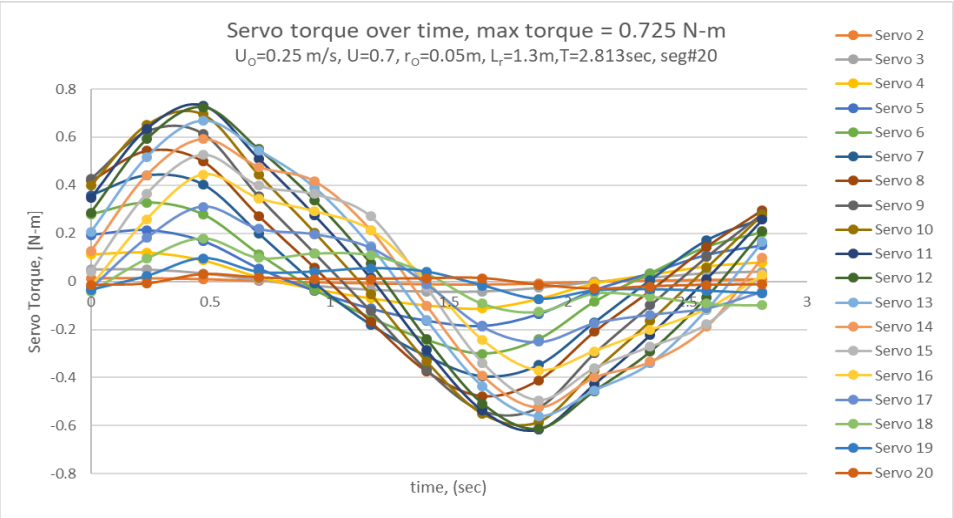

Fig. 17 Servo Torques of the model over time during free swimming

Along with all the above, global horizontal (A_X), transverse (A_Y) and angular (α_E) accelerations are also computed. The global accelerations over time are shown in Fig. 18.

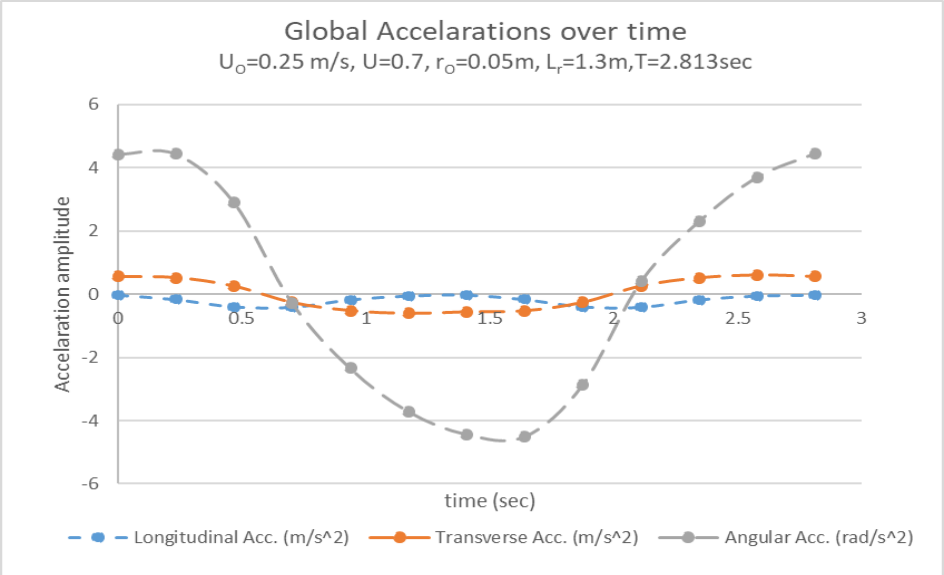

Fig. 18 Global Accelerations over time obtained by solving the equilibrium equations.

3.3.2. Tethered Swimming Case (Fixed-End Swimming)

This is a similar case to the untethered case, except that there are non-zero forces at forward point of the first segment. The forces and moments at the aft point of the last segment (tail end) remain zero. Due to the fixed condition, the global accelerations (A_x,A_y,α_E) of the body are zero. The internal acceleration ($\dot{u}_{x,1}$, $\dot{u}_{y,1}$) and velocity ($u_{x,1}$, $u_{y,1}$) of the first segment, that is fixed are also taken as zero.

$$\begin{aligned} A_x &= 0 & F_{x,N+1} &= 0 \\ A_y &= 0 & F_{y,N+1} &= 0 \\ \alpha_E &= 0 & M_{N+1} &= 0 \end{aligned} \tag{30}$$

Where, *N* is the total number of segments. This case predicts the maximum torque, which needs to be maintained by the servo actuators to obtain a specified motion.

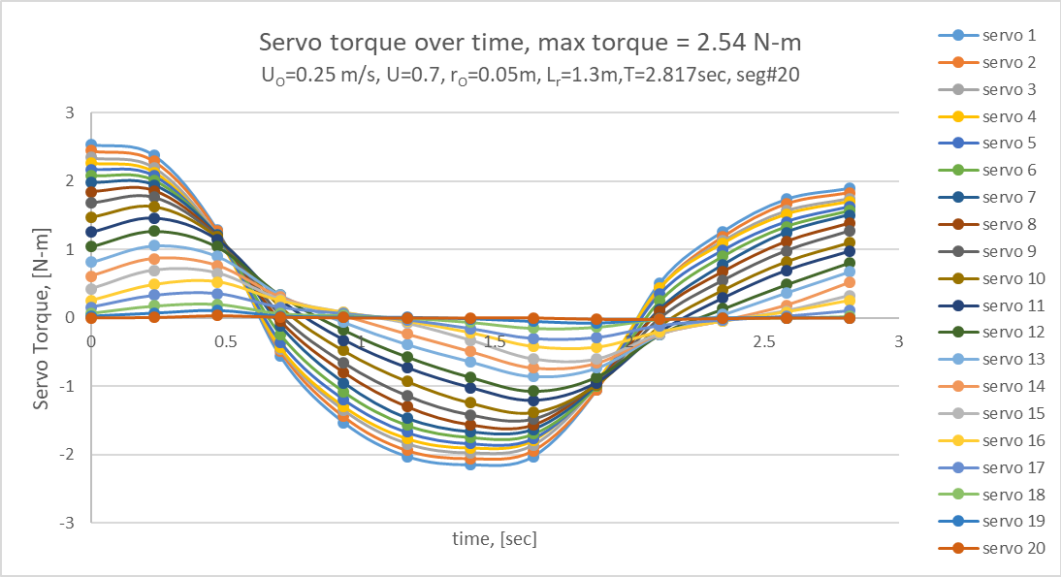

Fig. 19 Servo torques of the model over time when an end is fixed

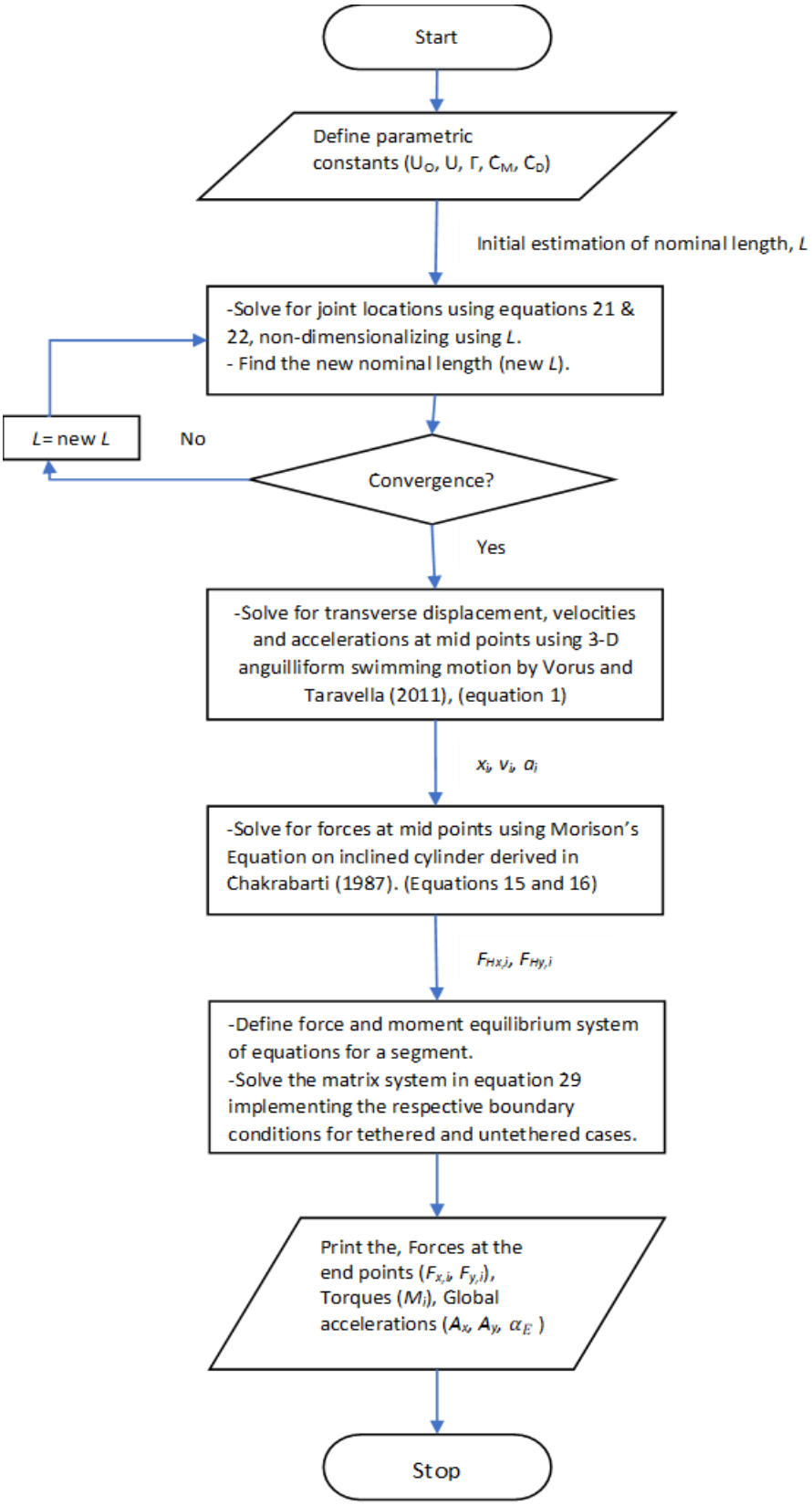

Fig. 20 Flow Process of the numerical method based on Morison's equation.

4. Comparison and Analysis

4.1. Analysis for Self-propulsion speed

This method helps us to identify the desired advance speed that could be attained by the robot during the run. This speed is called the self-propulsion speed. At this speed, the performance of the body is effectively high, and the robot tries to possess the desired ideal motion. In this case, the total longitudinal force (Thrust + Drag) becomes zero. This longitudinal force (F_x) is the mean of the total forces in the horizontal direction at different time steps in a cycle of motion calculated using Morison's equation (18).

$$F_x = \frac{1}{N}\sum_{i=0}^{N-1} F_{Hx,i} \tag{31}$$

Where N is the number of time steps.

The characteristics of the forward speed are computed by varying different parameters (coefficient of drag (C_D), displacement amplitude (Γ), wave speed (V=0.25/U)) are tested.

4.1.1. Coefficient of drag (C_D)

Forward speed decreases with drag coefficient. The slope of the thrust curves decreases, and the curves tend to flatten at low drag coefficients. Fig. 21 shows that, at an advance speed of 0.25 m/s, all the curves intersect as the Morison's drag is zero.

The self-propulsion speed significantly changes with the drag coefficient. Table 3 shows that the forward speed of the body varies approximately linearly with the drag coefficient. And the mean thrust at zero speed varies quadratically with C_D.

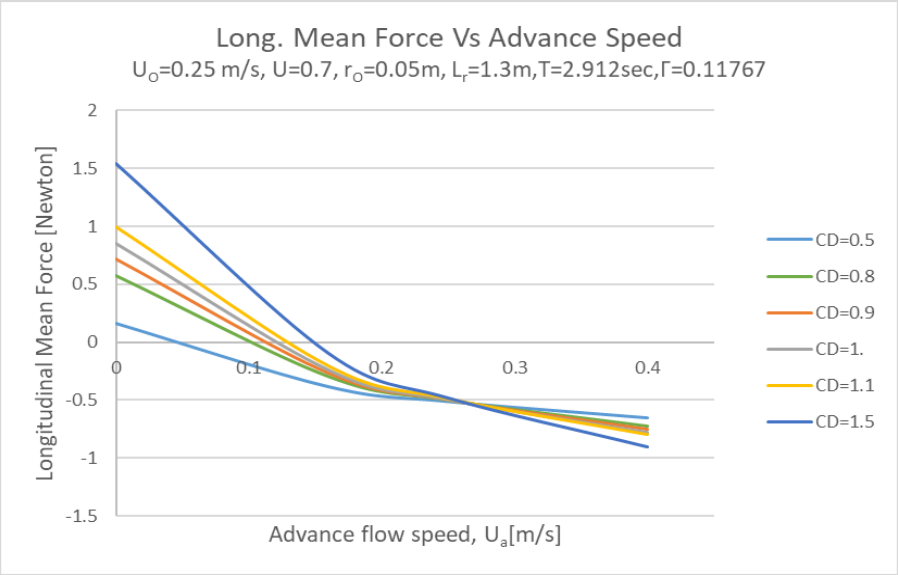

Fig. 21 Mean Longitudinal for a cycle of motion over time for varying coefficient of drag C_D at a flow speed of 0.25m/s

Table 3 Computed characteristics for all drag coefficients

Drag Coefficient	0.5	0.9	1	1.1	1.5
Self-swimming velocity (m/s)	0.05	0.115	0.125	0.13	0.15
Mean Thrust at 0m/s	0.2	0.7	0.9	1	1.5

The experimental data is recorded at four advance speeds mentioned in Table 4, maintaining the advance ratio, form and the motion constant.

Table 4 Table of advance ratio and speed considered to compare and analyze to get the self-propulsion speed

Ideal Speed, U_O [m/sec]	**Advance Ratio, U**	**Advance speed, U_a [m/sec]**	**Wave speed, V [m/sec]**
0.25	0.7	0.	0.357
0.25	0.7	0.16	0.357
0.25	0.7	0.25	0.357
0.25	0.7	0.4	0.357

Potts (2015) experimentally measured the velocities and accelerations of NEELBOT-1.1 by PIV testing. In this process, apart from the robot wake and velocities, the total thrust and drag forces are observed using the load-cell measurements. Fig. 22 shows the installation and experimental setup of the equipment in the towing tank.

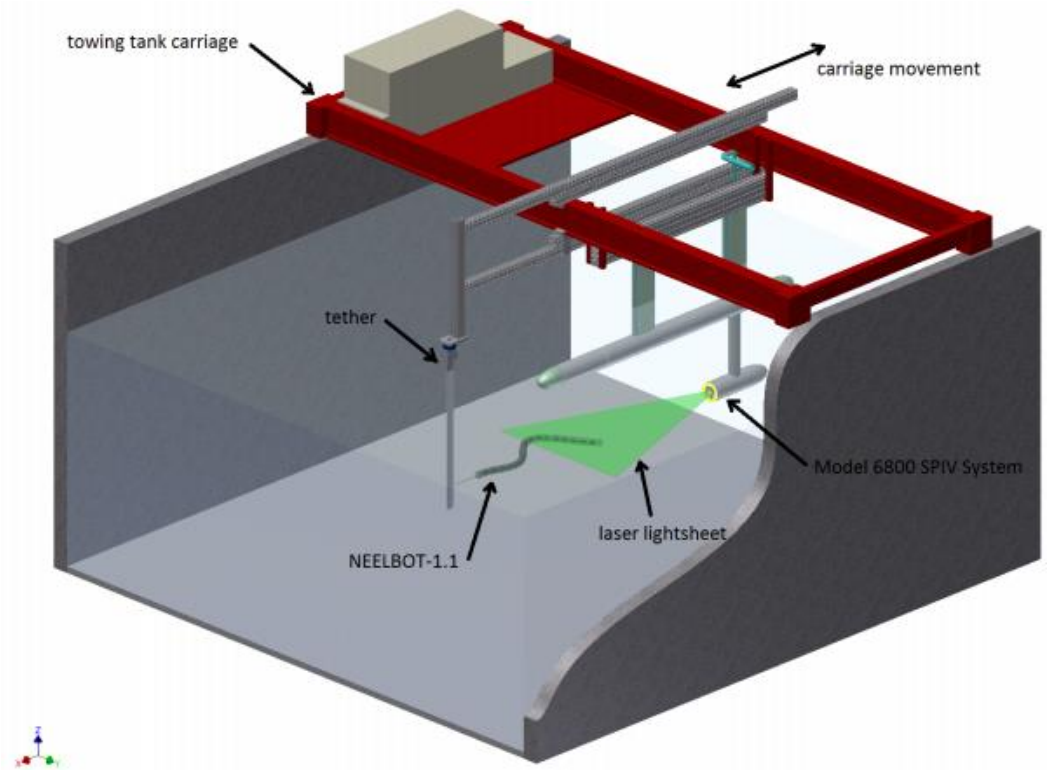

Fig. 22 Rendering of PIV equipment installed on UNO Towing Tank carriage of NEELBOT-1.1 and its tether. (Source: Potts (2015), Figure 4.1)

In this study, the theoretically computed mean thrusts are compared to the experimental results measured from the load cell. To compute the forces using Morison's equation, the coefficient of added mass of C_M=1.4 and the coefficient of drag of C_D=0.9 are selected to get the desired results.

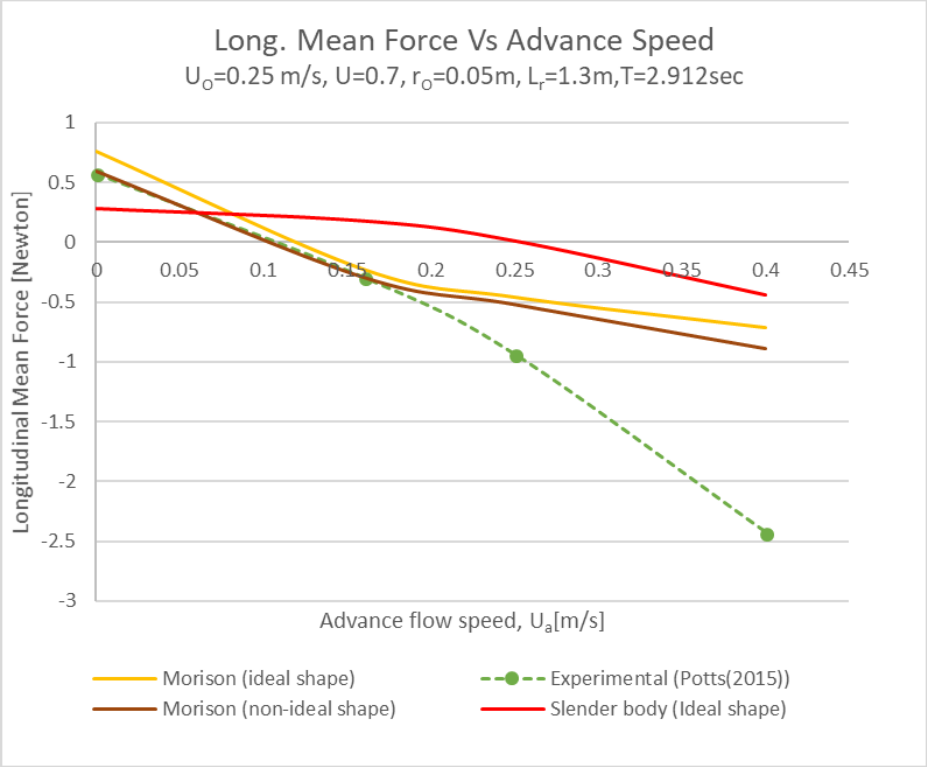

Fig. 23 Longitudinal force Vs. Advance speed (U_o) for 4 cases (Computed ideal flow-Morison's Equation, computed non-ideal flow-Morison's Equation, computed ideal flow-slender body theory, Experimental)

Unfortunately, Fig. 23 shows that the mean force computations by slender body theory are higher than the measured results. Morison's equation (with C_M=1.4, C_D=0.9) for non-ideal shape is able to predict the mean thrust values at low velocities.

4.1.2. Wave Speed (V)

Morison's equation does not exactly replicate the results of longitudinal force measured from NEELBOT-1.1 at higher speeds but, matches closely at lower speeds. Computations are run varying the advance ratios and the flow speed to analyze the behavior and performance of the model in various conditions by maintaining a constant motion and form. The ideal shape for the advance ratios of 0.4, 0.5, 0.6, 0.7 and 0.8 at different time steps are shown below from Fig. 24 through Fig. 28.

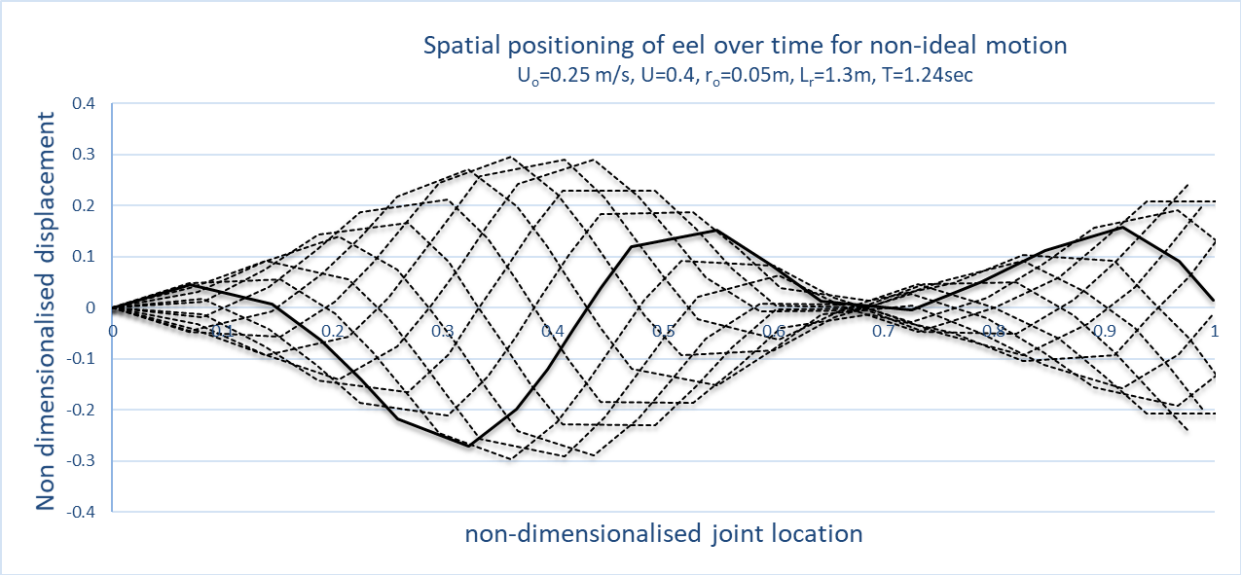

Fig. 24 Spatial position of Eel in non-ideal motion for 12 evenly spaced time steps for an advanced ratio of 0.4 and advance speed of 0.25m/s.

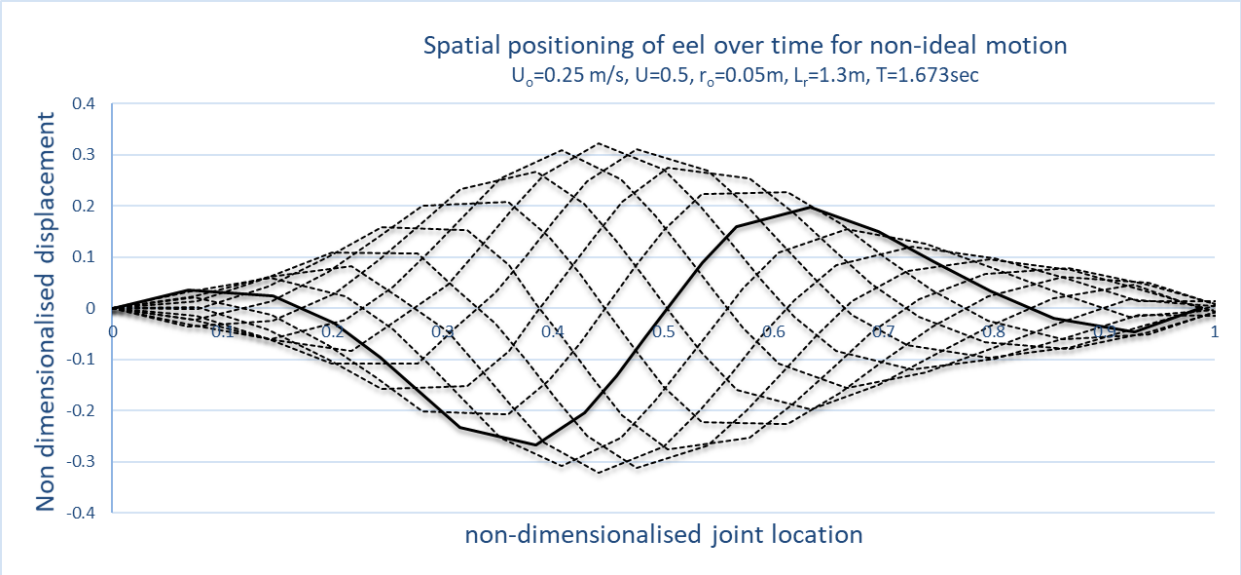

Fig. 25 Spatial position of Eel in non-ideal motion for 12 evenly spaced time steps for an advanced ratio of 0.5 and advance speed of 0.25m/s.

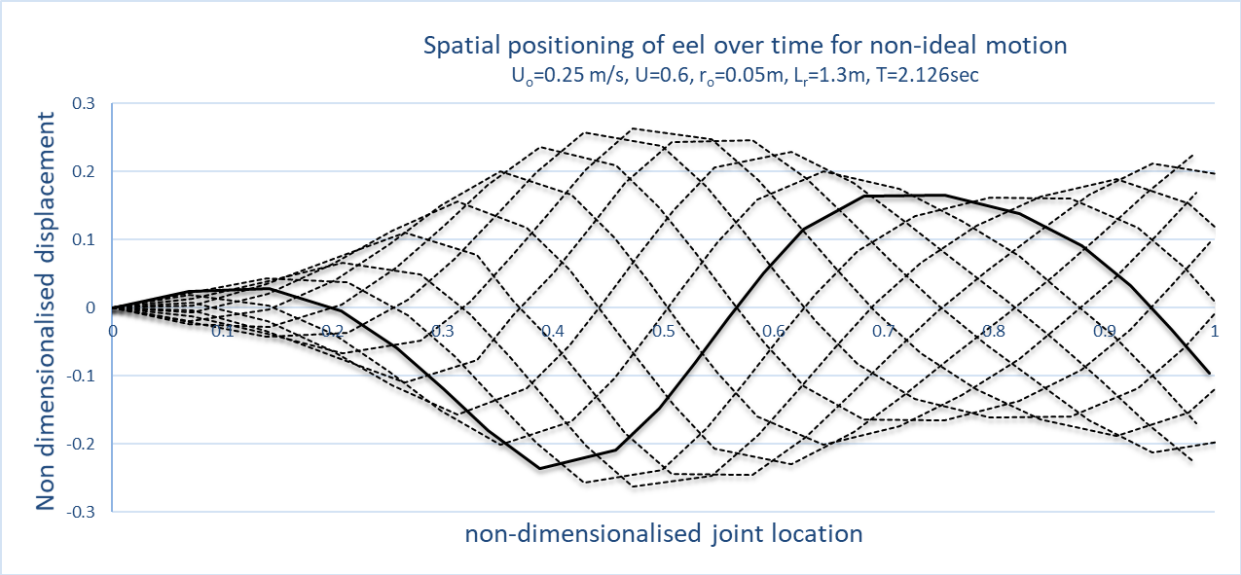

Fig. 26 Spatial position of Eel in non-ideal motion for 12 evenly spaced time steps for an advanced ratio of 0.6 and advance speed of 0.25m/s.

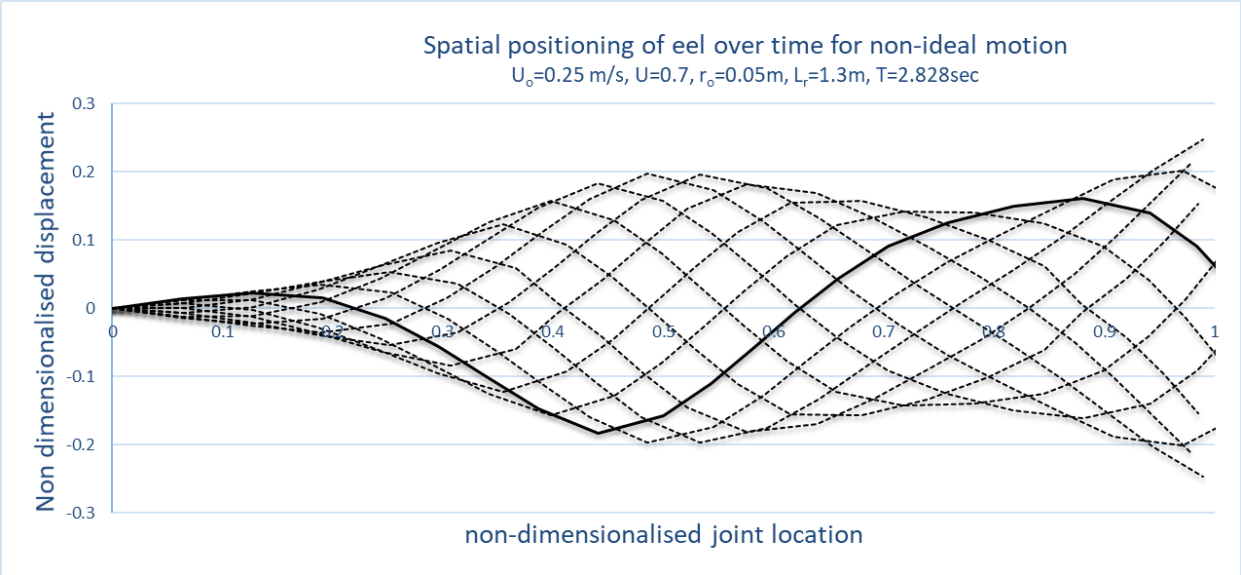

Fig. 27 Spatial position of Eel in non-ideal motion for 12 evenly spaced time steps for an advanced ratio of 0.7 and advance speed of 0.25m/s.

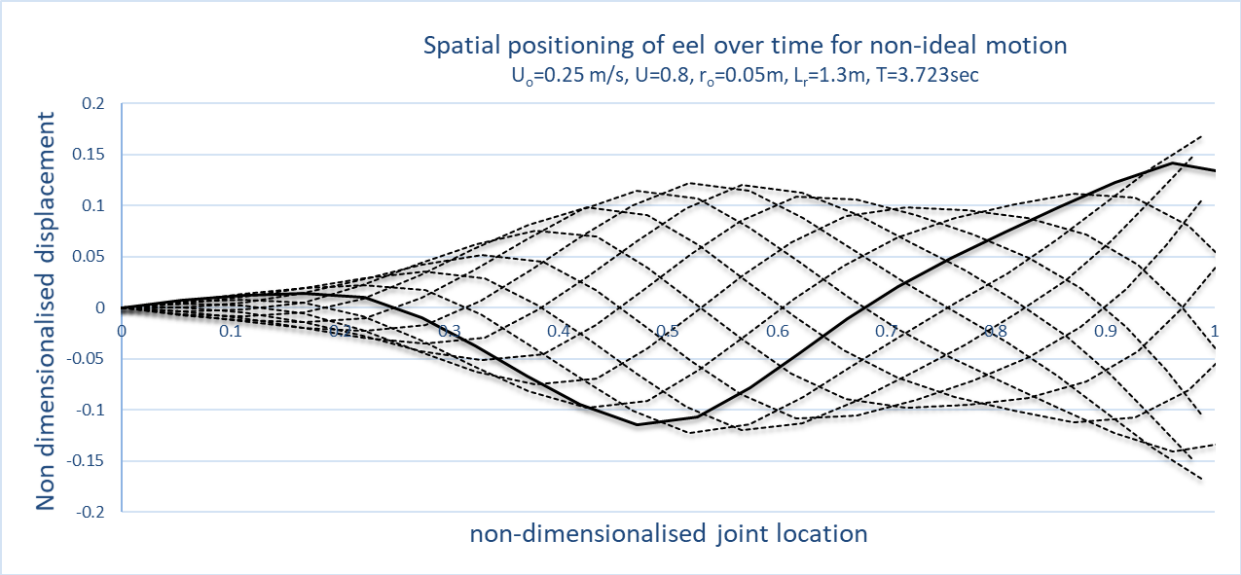

Fig. 28 Spatial position of Eel in non-ideal motion for 12 evenly spaced time steps for an advanced ratio of 0.8 and advance speed of 0.25m/s.

Below, Fig. 29 is a plot of the longitudinal forces over the flow speed. At U=0.5, the body reaches its local maximum forward speed. Physically, in this condition (U=0.5), the wave speed is twice the nominal flow speed, the nominal length (*L*) is equal to half the wave length as shown in Fig. 25.

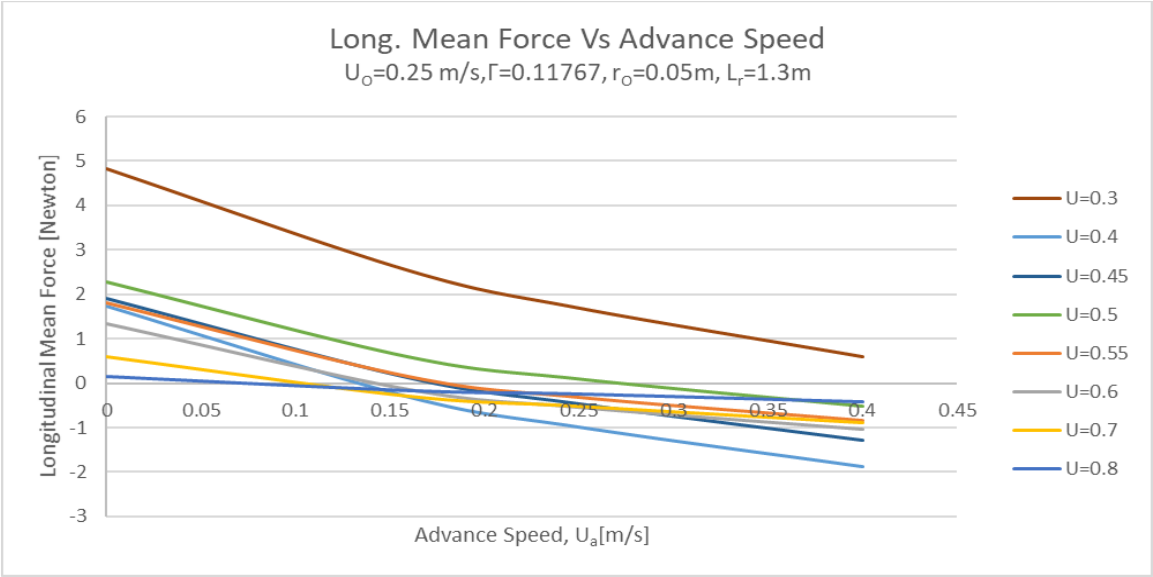

Fig. 29 Mean Longitudinal for a cycle of motion over time for varying advance ratio U at a flow speed of 0.25m/s

4.1.3. Displacement amplitude (Γ)

Fig. 30 is a plot of the longitudinal force over advance speed (U_a) maintaining the advance ratio constant (U=0.7) and varying the displacement amplitude (*Γ*). Interestingly, all the curves for different displacement amplitude meet at the same point on the horizontal axis. This explains that the self-propulsion speed of the robot is independent of the displacement amplitude, which is contrary to the results of the slender body theory of Vorus and Taravella (2011).

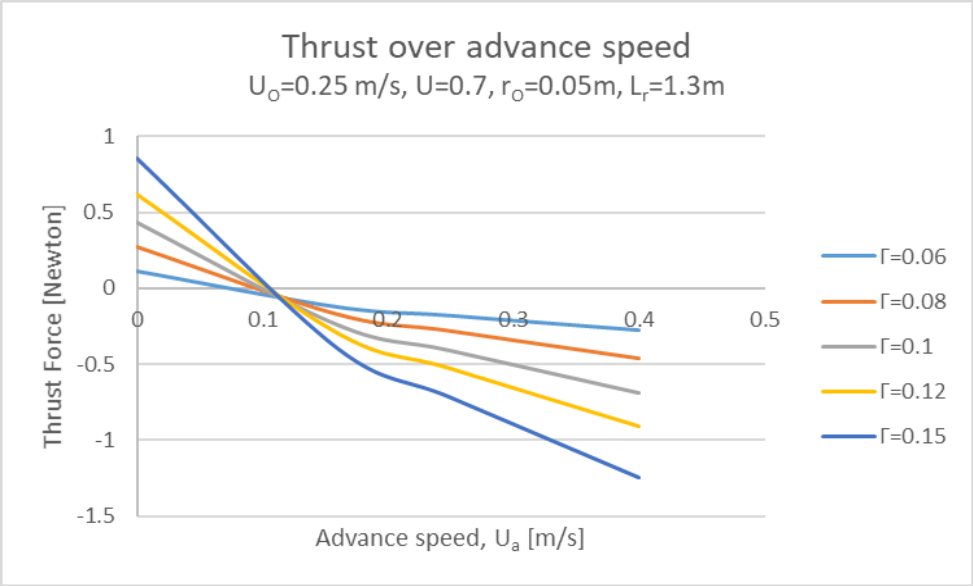

Fig. 30 Mean Longitudinal for a cycle of motion over time for varying displacement amplitude **Γ** at a flow speed of 0.25m/s

From the above two cases (one maintaining constant oscillating amplitude and the other maintaining constant wave speed), it can be inferred that every advance ratio is designated with a unique self-propulsion speed. It increases with the advance ratio up to a value of 0.5 and then decreases. This property is shown in Fig. 31.

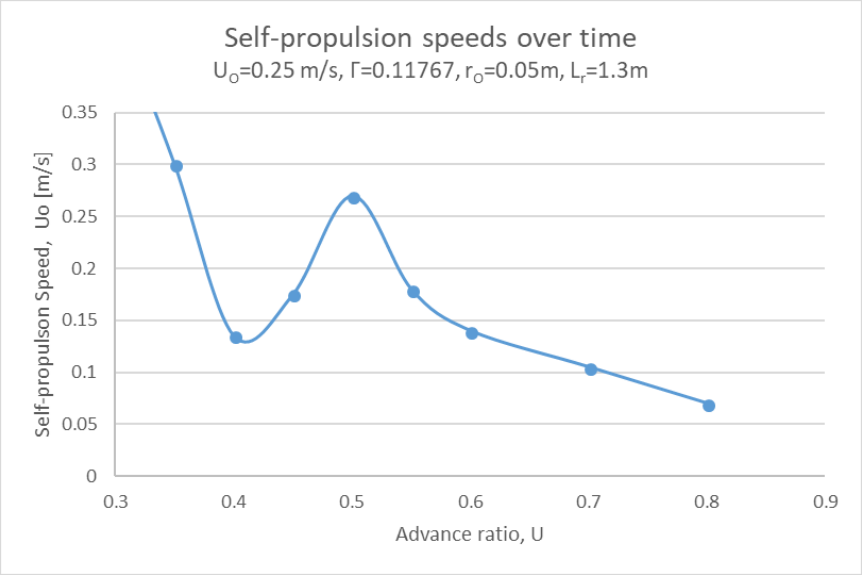

Fig. 31 Summary of Self-propulsion speeds over time considering the parameters in Table 2.

4.2. Comparison of torques at servo joints

Torque predictions by each servo motor are required to adequately size the motors. Torques at each servo motor for a tethered condition at an advance speed of 0.25 m/s are calculated using Morison's equation and slender body theory. Fig. 32 and Fig. 33 show the plots of servo torques for each servo joint over time. The predictions show that the maximum servo torque occurs at the servo index 2.

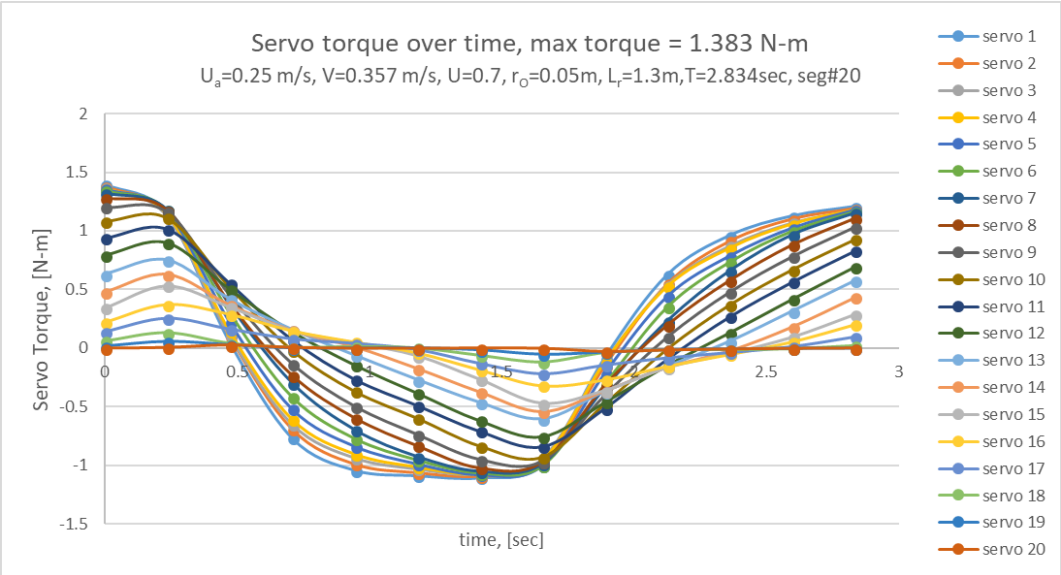

Fig. 32 Prediction of Servo torques over time at each servo joint using Morison Equation for computing forces.

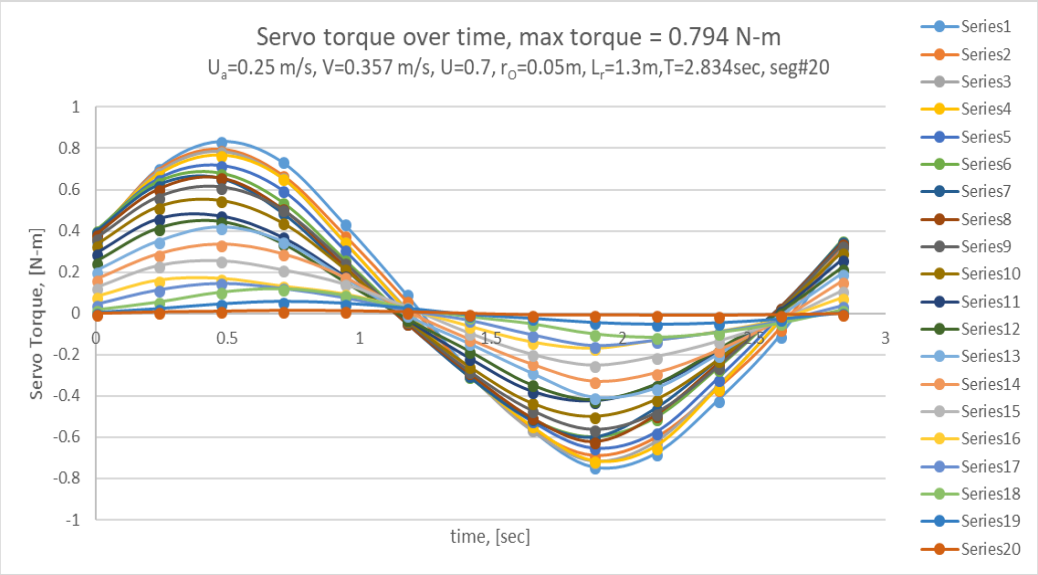

Fig. 33 Prediction of Servo torques over time at each servo joint using slender body theory method for computing forces.

The speed-torque curves of the servo motor 2 is shown in Fig. 34. According to the vendor specifications, the stall torque is 2.4 N-m and the maximum angular velocity is 408 deg/s. The gray line represents the limit specifications of Dongbu Herkulex DRS-0201. The blue line is the torque (1.383 N-m) predicted using Morison's equation to overcome the drag at a velocity of 0.25 m/s for non-ideal motion. Fig. 35 illustrates that at higher wave speed this method predicts torques which lies outside the stall torque limits provided by the vendor. This shows that the required velocity cannot be achieved by the current servo motors.

Whereas, the slender body theory predicts the maximum torque to be 0.794 N-m which is way less than the limitations provided. Experimental results of Potts (2015) show that NEELBOT-1.1 could not be run at the required speed and predicted the reason behind to be insufficient torques. Therefore, Morison's equation is expected to well predict the torques.

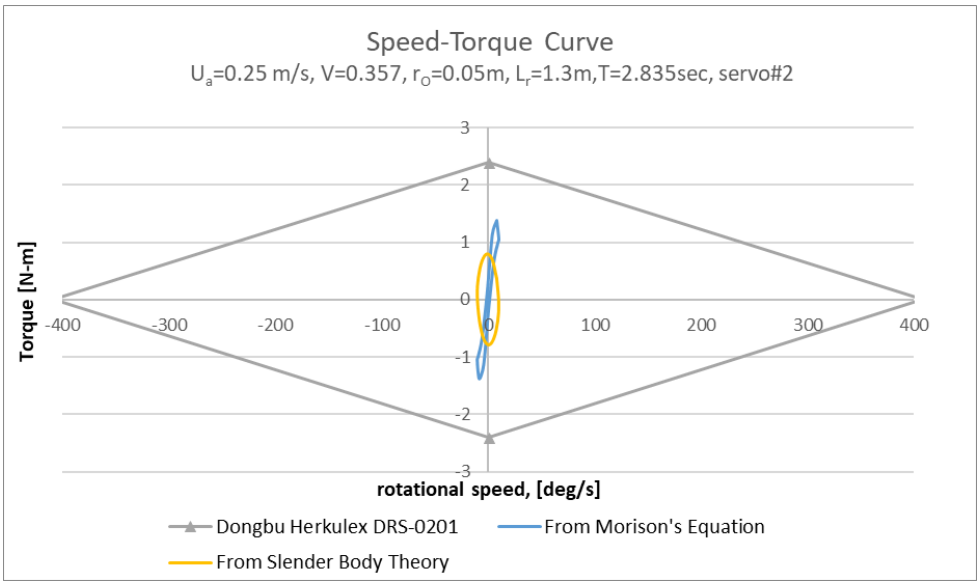

Fig. 34 Rotational Speed-Torque curve for Dongbu Herkulex DRS-0201 computed using Morison's equation and slender body theory at a nominal speed of 0.25m/s.

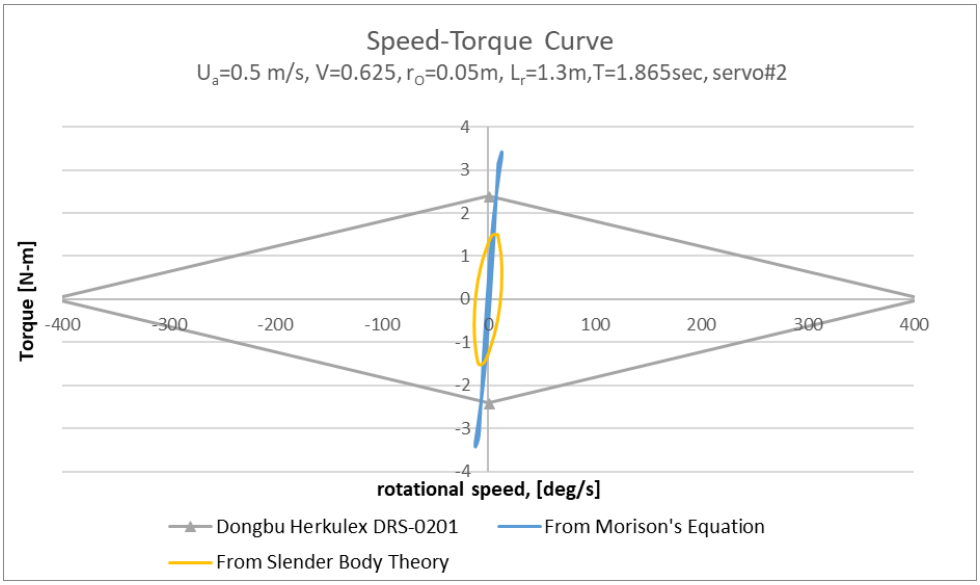

Fig. 35 Rotational Speed-Torque curve for Dongbu Herkulex DRS-0201 computed using Morison's equation and slender body theory at a nominal speed of 0.5m/s.

The rotational speed-torque curves of the nineteen servo actuators at the self-swimming speed (U_a) of 0.105m/s are predicted using Morison's equation and slender body theory for a tethered condition. The motion has highest efficiency at this speed. These plots are included in Appendix 1.

5. Conclusion

It is a very challenging task to analyze the hydrodynamics of an anguilliform swimming motion. Unlike a ship, these bodies oscillate and are not uniform throughout their length. Computational analysis of the anguilliform motion becomes difficult when compared to experimental analysis. The discontinuities at the joints make it very challenging to obtain the hydrodynamic properties of these bodies.

The theoretical ideal anguilliform swimming motion is classified as “wakeless” with zero circulation around the body by Vorus and Taravella (2011). This method is theorized to produce accelerations of the hydrodynamic added mass in the vicinity of the body for a reactive swimming technique.

In this study, an effort was made to compute the hydrodynamic forces of the anguilliform swimming robot using Morison’s equation. The experimental results of the twenty-segmented NEELBOT-1.1 were replicated using the computational analysis. The entire process can be summarized in the following three steps: 3-D ideal anguilliform swimming motion is applied to predict the robotic motion; Morison’s equation is used to analyze the hydrodynamics of the eel body and combination of the above two theories in an ideal motion case is used to determine the velocity at which the robot can run at the expected forward velocity.

The segments’ joint locations for the discretized body in this motion are computed iteratively for twelve equally spaced time steps of a path cycle using 3-D displacement equation from Vorus and Taravella (2011). For computational purposes, each segment of the body is considered as an individual inclined cylinder. The flow stream velocity and the transverse velocities and accelerations from the ideal flow theory are used to calculate the hydrodynamic forces using Morison’s Equation. The mean thrust for every cycle is relatively well predicted.

A comparison of torques of the servo motors is made between the computation with Morison's equation and slender body theory in reference to the experimental results from Potts (2015). According to Morrison's method, the torques required to overcome the drag at the self-propulsion velocity of 0.105m/s for non-ideal motion in a tethered condition are greater than the predictions from slender body theory. Fig. 35 explains that higher nominal speeds cannot be attained by the current servo motors as the curve lies outside the vendor stall torque limits. At the self-swimming speed, the percentage difference between the torques computed using the two methods decreased. Though, Morison's equation still had higher predictions due to the significant drag component involved in this method unlike the slender body theory.

A series of comparisons are made by changing the coefficient of drag (C_D), speeds (U_O, V) and displacement amplitude (Γ). Forward speed decreases with a decrease in the drag coefficient. The slope of the thrust curves decreases, and the curves tend to flatten at low drag coefficients. The mean thrust at zero speed decreases approximately quadratically and the self-propulsion speed varies linearly with the drag coefficient. An added mass coefficient of 1.4 and a drag coefficient of 0.9 are used in the analysis to replicate the experimental results. Morison's equation is more flexible due to the variable factor of added-mass and drag coefficients.

The experimental thrust values for an advance ratio of 0.7 are compared to three cases: Morison's equation in ideal design motion, Morison's equation in non-ideal motion and slender body theory in ideal motion. The mean thrust forces are well predicted using Morison's equation in ideal design motion at low velocities.

At higher velocities, the thrust forces produced in the downstream direction dominate the drag forces in the upstream direction. Whereas, at lower velocities drag forces are stronger. At a downstream

velocity, the induced thrust and drag forces come to equilibrium. This velocity is termed as self-propulsion velocity which is the vendor-desired velocity.

The self-propulsion velocities lie in the range of 0.1-0.25 m/s. Morison's equation predicts mean thrust with high accuracy at these low velocities. With an increase in the oscillating amplitude (Γ), an increase in the transverse lift is determined. This self-propulsion forward velocity is independent of the oscillating amplitude at a constant advance ratio. The self-propulsion speed is dependent on the advance ratio (U). It increases with the advance ratio up to a value of U=0.5 and then decreases as shown in Fig. 31. At an advance ratio of 0.5, the nominal length is equal to half of the wavelength.

In conclusion, mean thrust, torque, and the self-propulsion speed are well predicted using Morison's equation. The self-propulsion speed is independent of the oscillating amplitude and changes with the advance ratio. Unfortunately, this method failed at higher velocities for predicting forces.

References

Apneseth, C. C., Day, A.H., Clelland, D. (2010). Hydrodynamics of an oscillating articulated eel-like structure. *Ocean Engineering*.

Breder. C.M., Jr. (1926). The locomation of fishes. *Zoologica*, 4:159-297.

Chakrabarti, S. K. (1987). *Hydrodynamics of Offshore Structures.* Computational Mechanics Publications.

Gray, J. (1936). Studies in animal locomation: Vi. the propulsive powers of the dolphin. *Journal of Experimental Biology*, 13(2):192-199.

Houssay, F. (1912). Forme, Puissance et Stabilite des Poissons. *A. Hermann et Fils, Paris.*, 372 p.

ITTC. (1957). Eigth Imternational Towing Tank Conference. Madrid: Canal de Experiencias Hidrodinamicas, El Pardo.

Lighthill, M. (1964). *Fourier Analysis and Generalized Functions.* Cambridge: Cambridge University Press.

Lighthill, M. (1970). Hydromechanics of aquatic animal propulsion. *Annual Review of Fluid Mechanics*, 44(2):265-301.

Lighthill, M. (1971). Large-amplitude elongated-body theory fish locomotion. *Proceedings of the Royal Society of London*, 179(1055):125-138.

Lighthill,M. (1960). Note on the swimming of slender fish. *Journal of Fluid Mechanics*, 9(2):305-317.

Morison, J. R., O'Brien, M. P., Johnson, J. W., and Schaaf, S.A. (1950). The force exerted by surface waves on piles. *Petroleum Transactions, AIME*, 189, 149-157.

Pettigrew, J. B. (1873). Animal Locomation. *H. S. King and Co., London*, 264 p.

Potts, J.B., III. (2015). *Developing and Testing an Anguilliform Robot Swimming with Theoretically High Hydrodynamic Efficiency.* New Orleans: scholarworks@uno.edu.

Taylor, G. (1552). Analysis of the swimming of long and narrow animals. *Proceedings of the Royal Society*, 214(1117):158-183.

Vorus, W. S. (2005). Swimming of the semi-infinite strip revisited. *Journal of Engineering Mathematics*, 51(1):35–55.

Vorus, W. S. and Taravella, B. M. (2011). Anguilliform fish propulsion of highest hydrodynamic efficiency. *Journal of Marine Science and Application*, 10(2):163–174.

Webb, P. W. (1975). In *Hydrodynamics And Energrtics of Fish Propulsion.* Ottawa: Bulletin of Fisheries Research Board of Canada.

Appendix

1. Results comparing torques of servo motors

The speed-torque plots of the nineteen servo motors employed in the robot to get the swimming speed of 0.105 m/s are shown in this section. These figures show the torques required by the servo actuators for maximum efficiency.

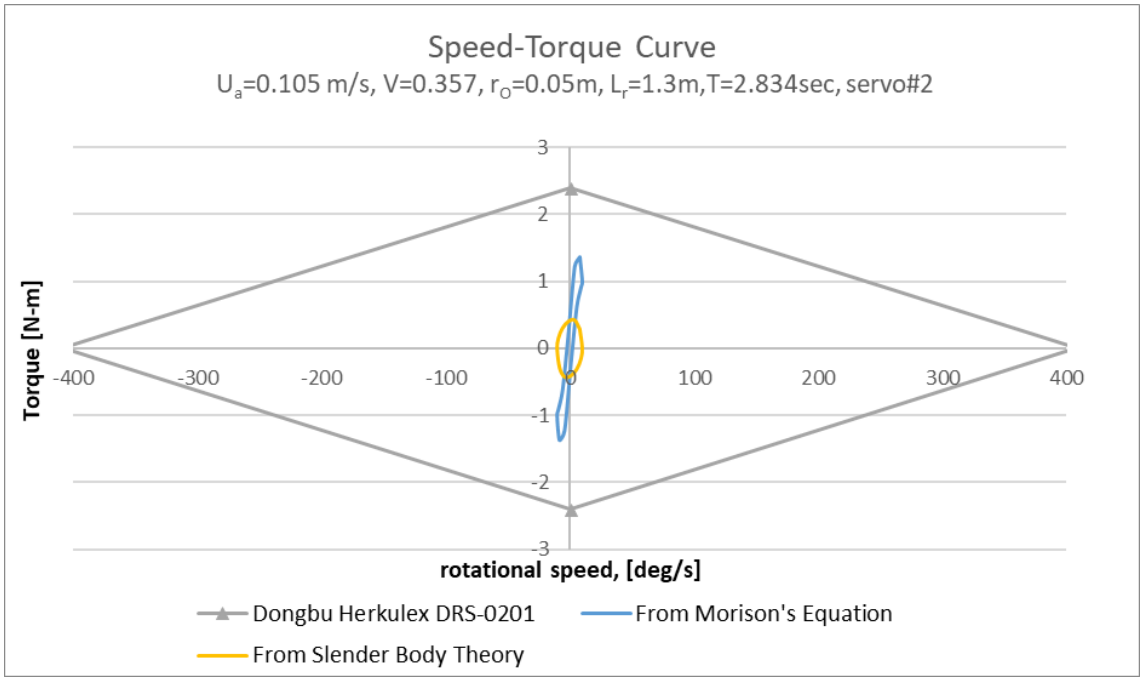

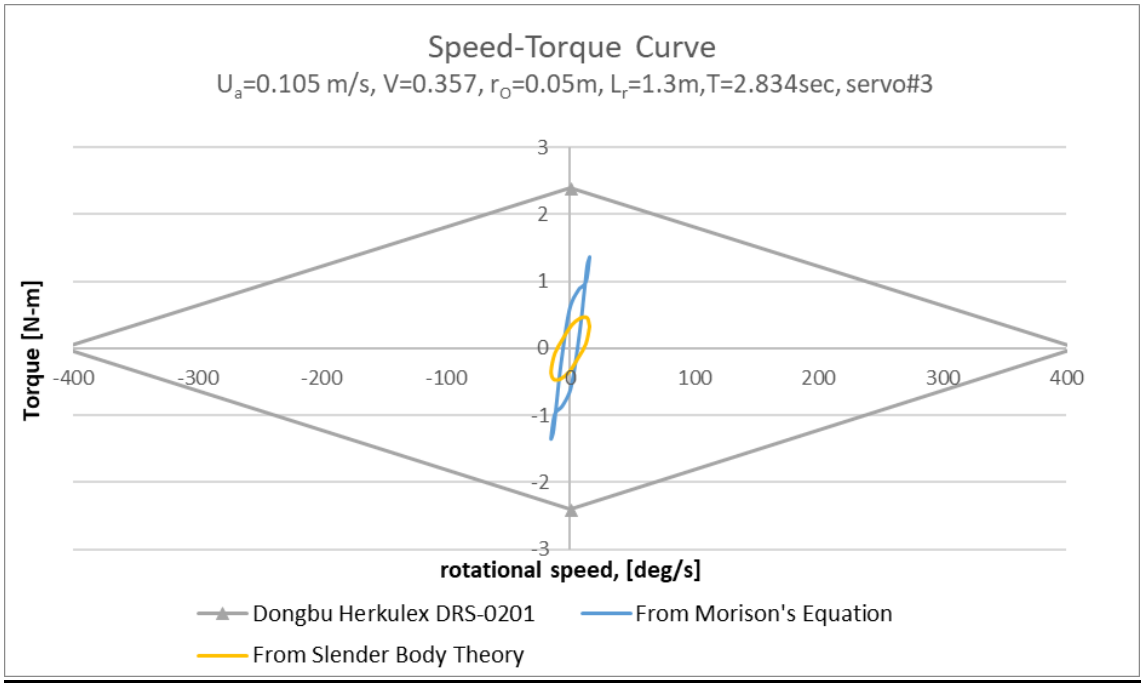
Speed-Torque Curve
U_a=0.105 m/s, V=0.357, r_O=0.05m, L_r=1.3m,T=2.834sec, servo#3
Torque [N-m]
3
2
1
0
-1
-2
-3
-400
-300
-200
-100
0
100
200
300
400
rotational speed, [deg/s]
Dongbu Herkulex DRS-0201
From Morison's Equation
From Slender Body Theory

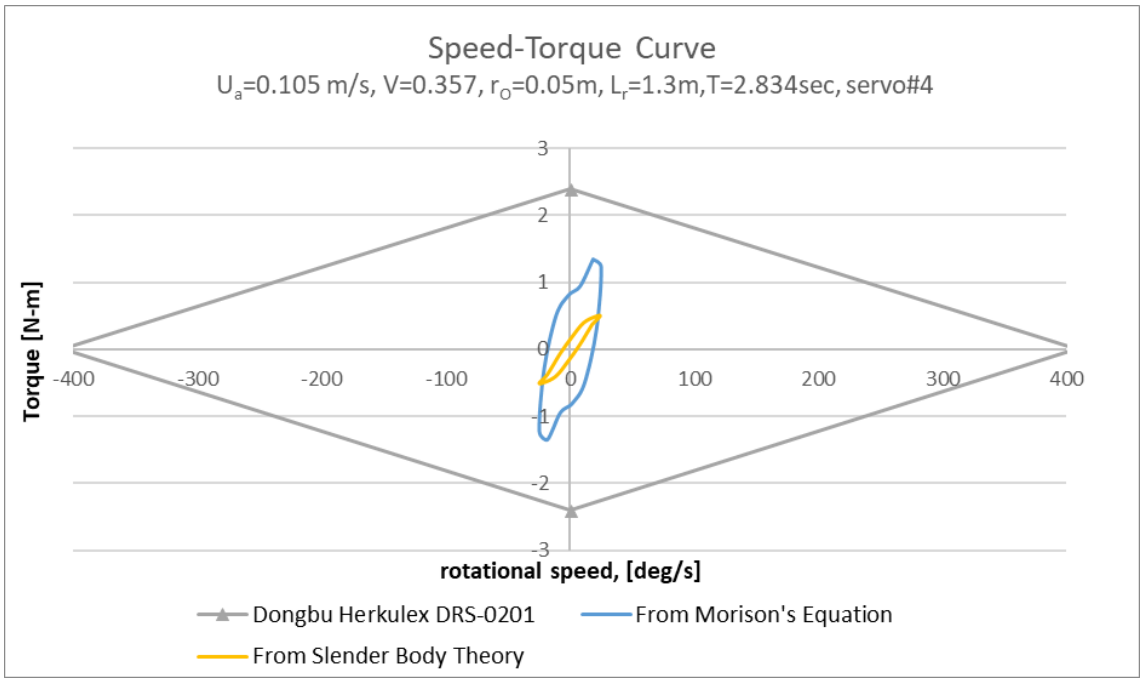
Speed-Torque Curve
U_a=0.105 m/s, V=0.357, r_O=0.05m, L_r=1.3m,T=2.834sec, servo#4
Torque [N-m]
3
2
1
0
-1
-2
-3
-400
-300
-200
-100
0
100
200
300
400
rotational speed, [deg/s]
Dongbu Herkulex DRS-0201
From Morison's Equation
From Slender Body Theory

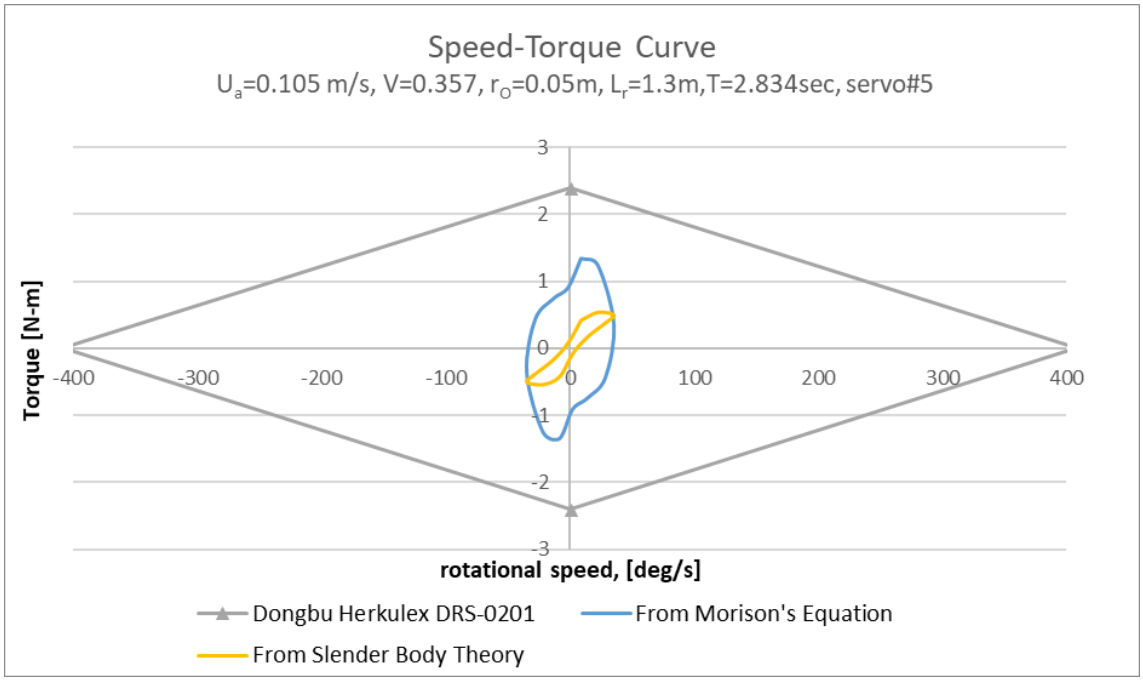
Speed-Torque Curve
U_a=0.105 m/s, V=0.357, r_O=0.05m, L_r=1.3m,T=2.834sec, servo#5
Torque [N-m]
rotational speed, [deg/s]
Dongbu Herkulex DRS-0201
From Morison's Equation
From Slender Body Theory

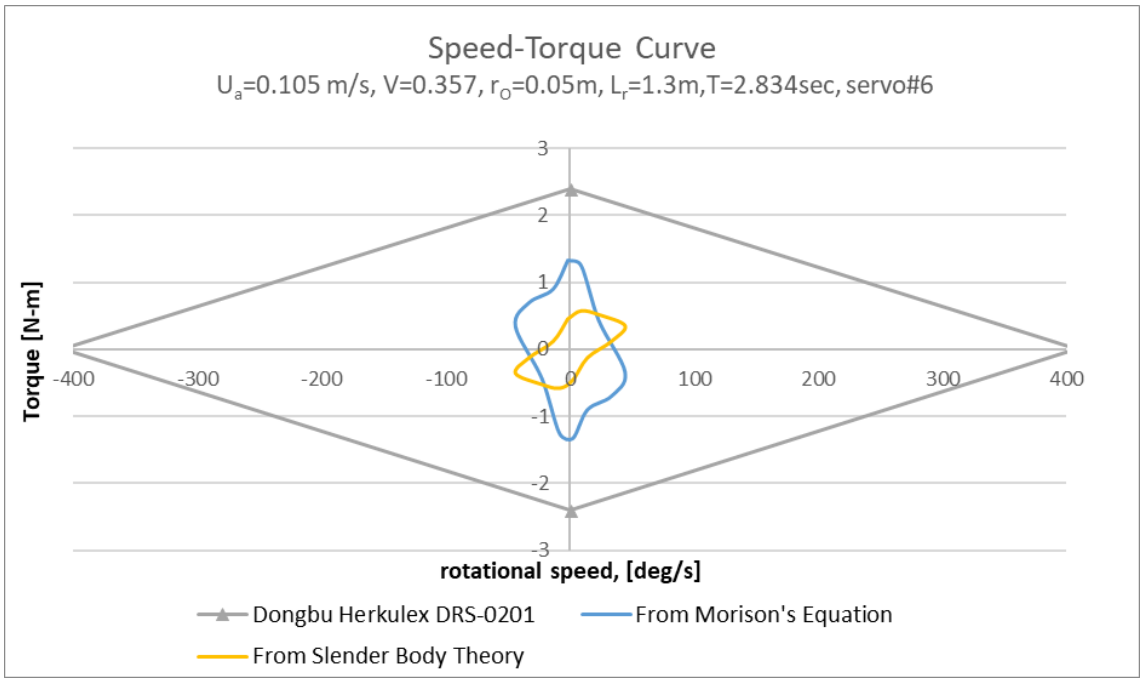
Speed-Torque Curve
U_a=0.105 m/s, V=0.357, r_O=0.05m, L_r=1.3m,T=2.834sec, servo#6
Torque [N-m]
rotational speed, [deg/s]
Dongbu Herkulex DRS-0201
From Morison's Equation
From Slender Body Theory

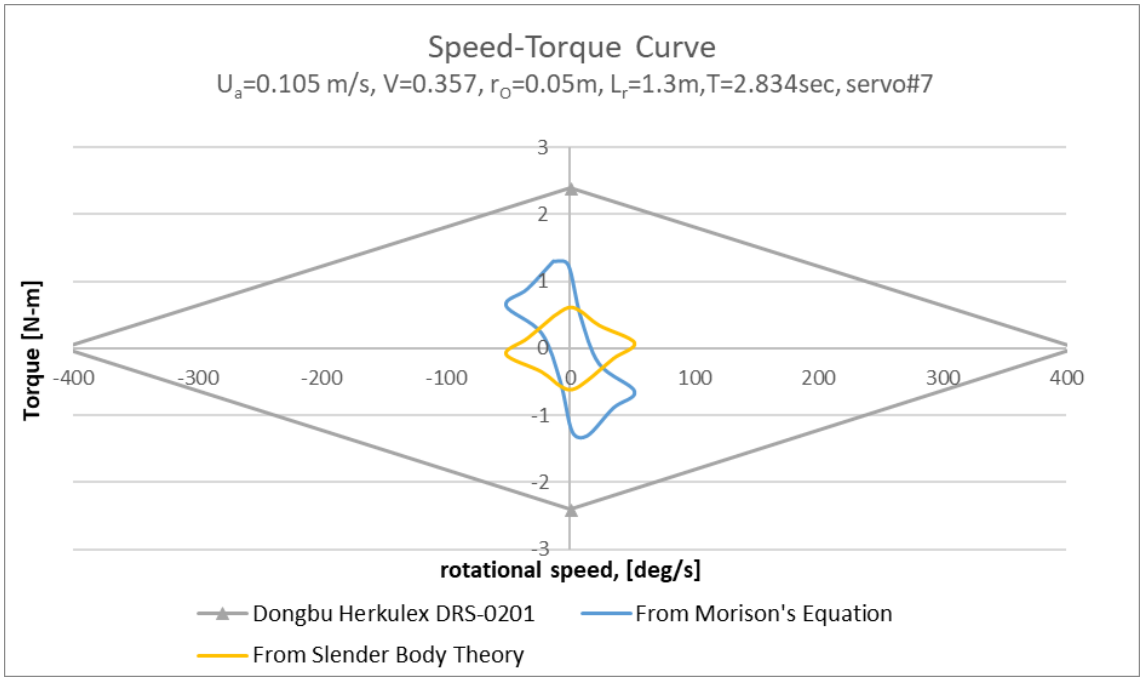
Speed-Torque Curve
U_a=0.105 m/s, V=0.357, r_O=0.05m, L_r=1.3m,T=2.834sec, servo#7
Torque [N-m]
3
2
1
0
-1
-2
-3
-400
-300
-200
-100
0
100
200
300
400
rotational speed, [deg/s]
Dongbu Herkulex DRS-0201
From Morison's Equation
From Slender Body Theory

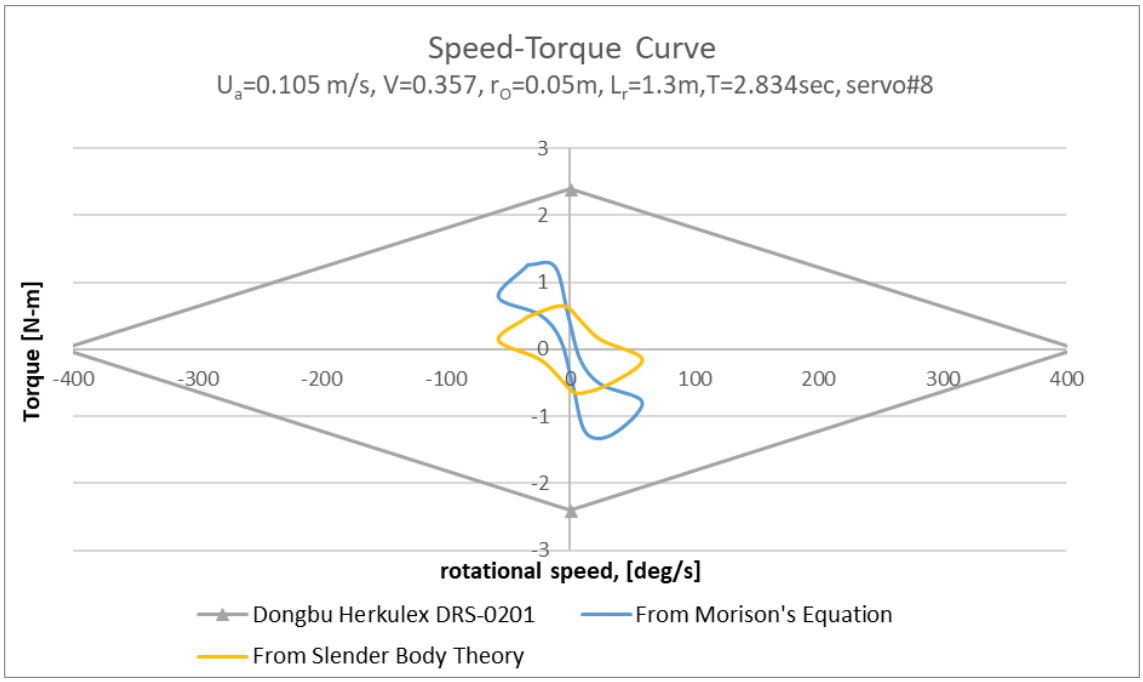
Speed-Torque Curve
U_a=0.105 m/s, V=0.357, r_O=0.05m, L_r=1.3m,T=2.834sec, servo#8
Torque [N-m]
3
2
1
0
-1
-2
-3
-400
-300
-200
-100
0
100
200
300
400
rotational speed, [deg/s]
Dongbu Herkulex DRS-0201
From Morison's Equation
From Slender Body Theory

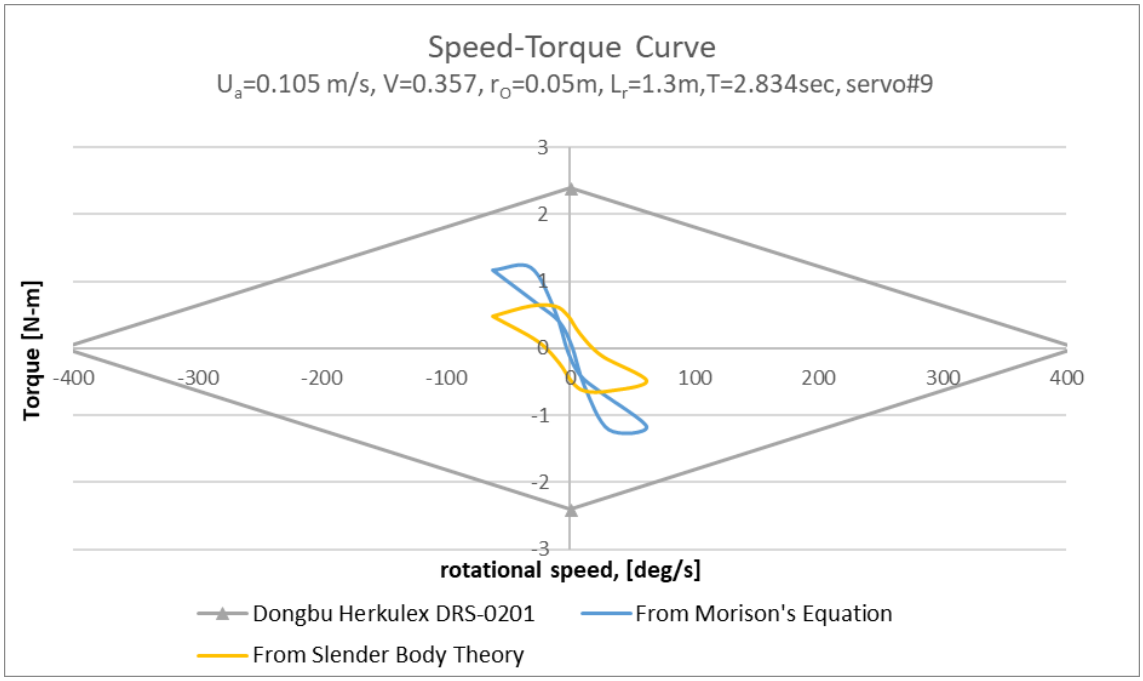
Speed-Torque Curve
U_a=0.105 m/s, V=0.357, r_O=0.05m, L_r=1.3m,T=2.834sec, servo#9
Torque [N-m]
rotational speed, [deg/s]
Dongbu Herkulex DRS-0201
From Morison's Equation
From Slender Body Theory

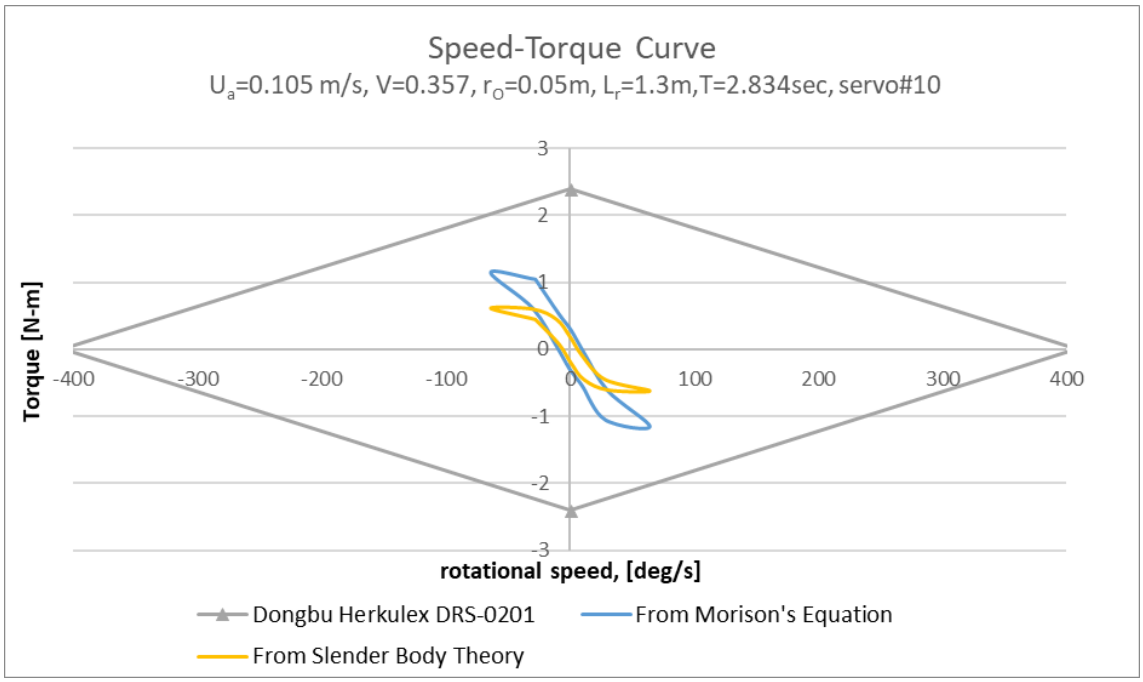
Speed-Torque Curve
U_a=0.105 m/s, V=0.357, r_O=0.05m, L_r=1.3m,T=2.834sec, servo#10
Torque [N-m]
rotational speed, [deg/s]
Dongbu Herkulex DRS-0201
From Morison's Equation
From Slender Body Theory

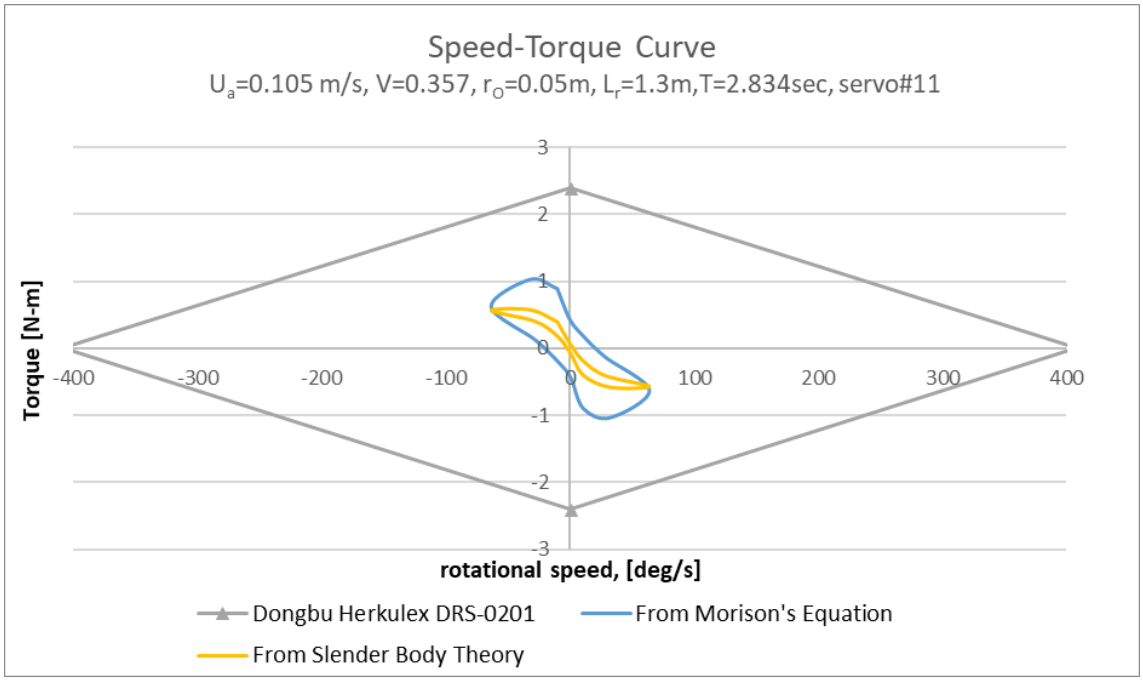
Speed-Torque Curve
U_a=0.105 m/s, V=0.357, r_O=0.05m, L_r=1.3m,T=2.834sec, servo#11
Torque [N-m]
3
2
1
0
-1
-2
-3
-400
-300
-200
-100
0
100
200
300
400
rotational speed, [deg/s]
Dongbu Herkulex DRS-0201
From Morison's Equation
From Slender Body Theory

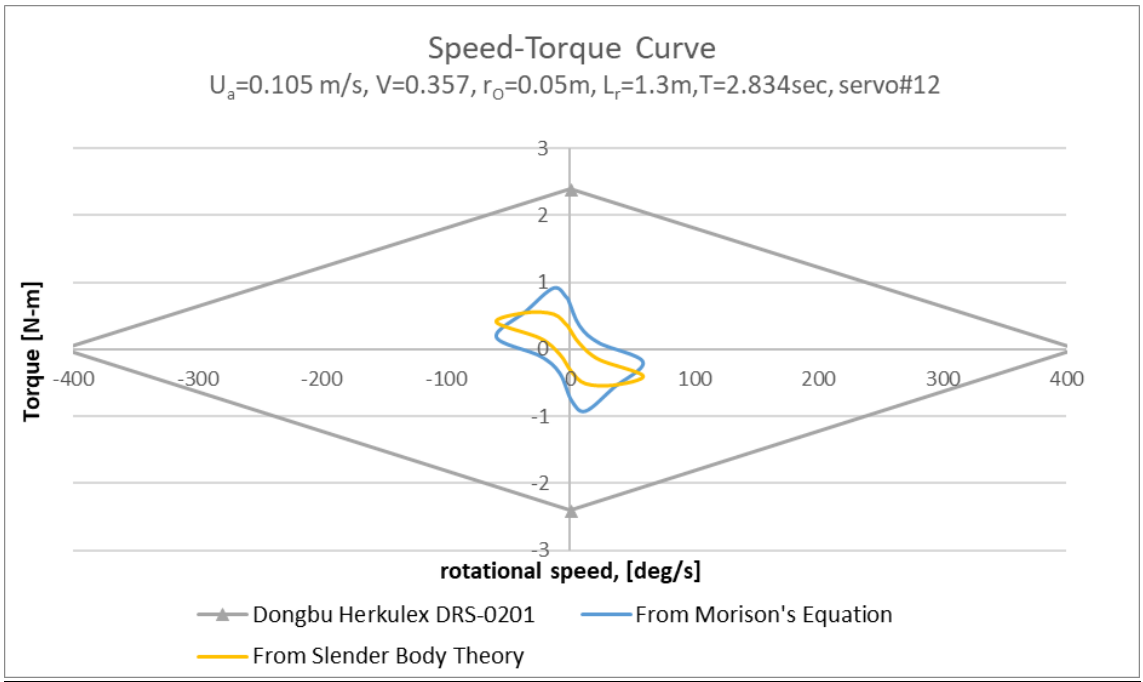
Speed-Torque Curve
U_a=0.105 m/s, V=0.357, r_O=0.05m, L_r=1.3m,T=2.834sec, servo#12
Torque [N-m]
3
2
1
0
-1
-2
-3
-400
-300
-200
-100
0
100
200
300
400
rotational speed, [deg/s]
Dongbu Herkulex DRS-0201
From Morison's Equation
From Slender Body Theory

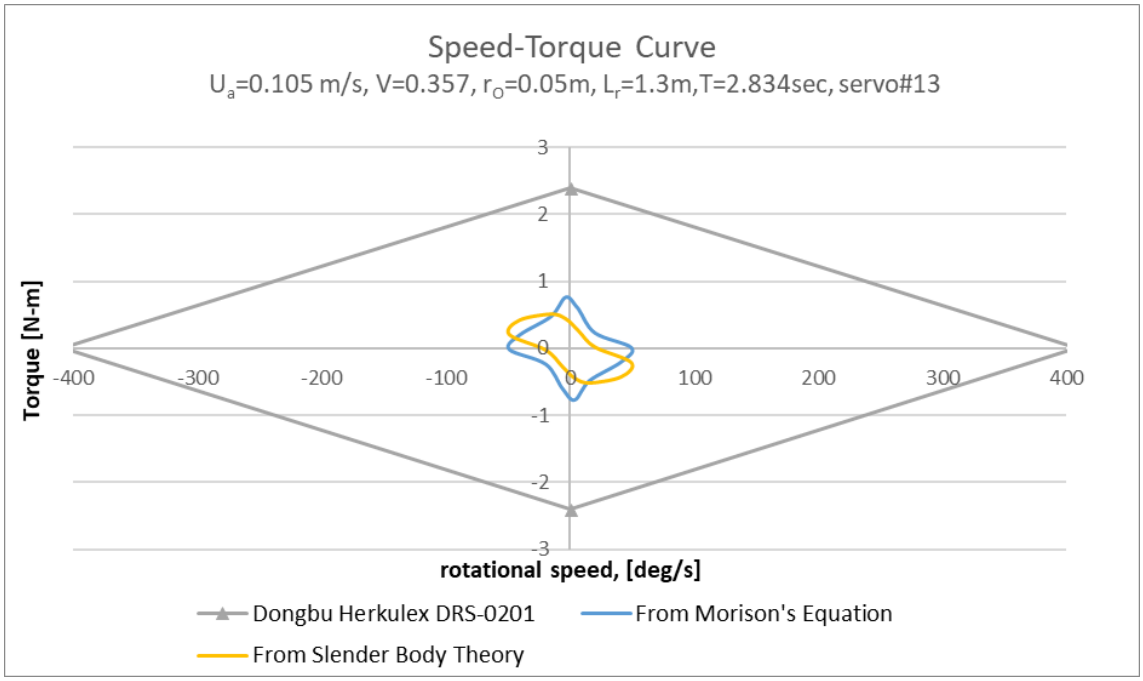
Speed-Torque Curve
U_a=0.105 m/s, V=0.357, r_O=0.05m, L_r=1.3m,T=2.834sec, servo#13
Torque [N-m]
3
2
1
0
-1
-2
-3
-400
-300
-200
-100
0
100
200
300
400
rotational speed, [deg/s]
Dongbu Herkulex DRS-0201
From Morison's Equation
From Slender Body Theory

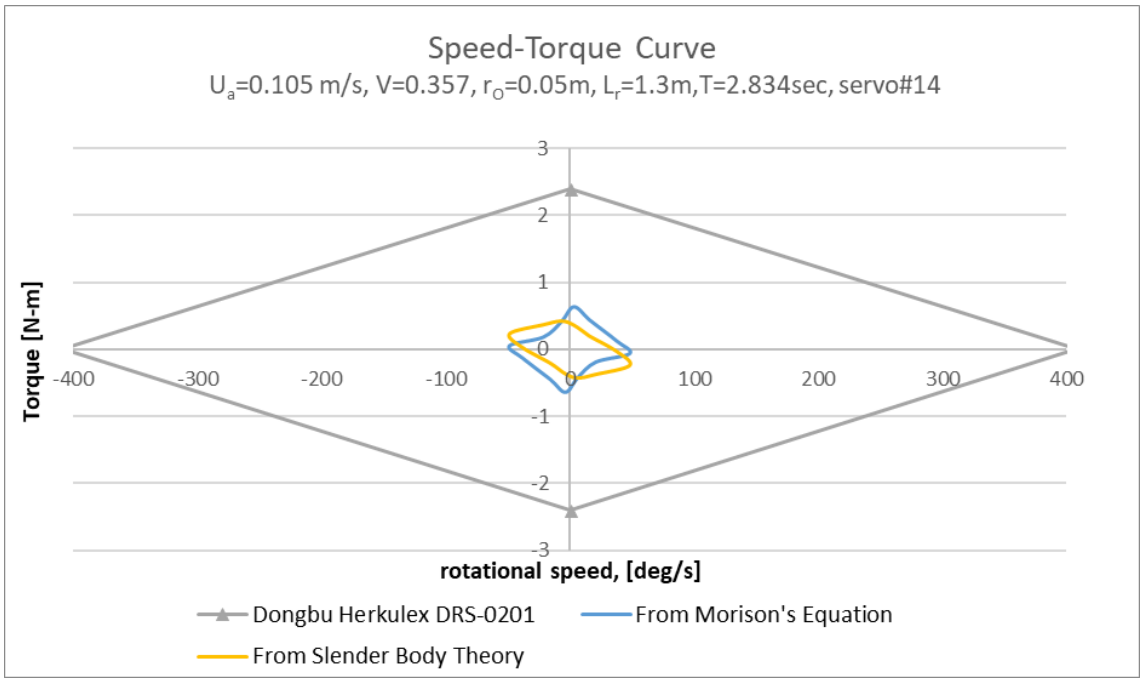
Speed-Torque Curve
U_a=0.105 m/s, V=0.357, r_O=0.05m, L_r=1.3m,T=2.834sec, servo#14
Torque [N-m]
3
2
1
0
-1
-2
-3
-400
-300
-200
-100
0
100
200
300
400
rotational speed, [deg/s]
Dongbu Herkulex DRS-0201
From Morison's Equation
From Slender Body Theory

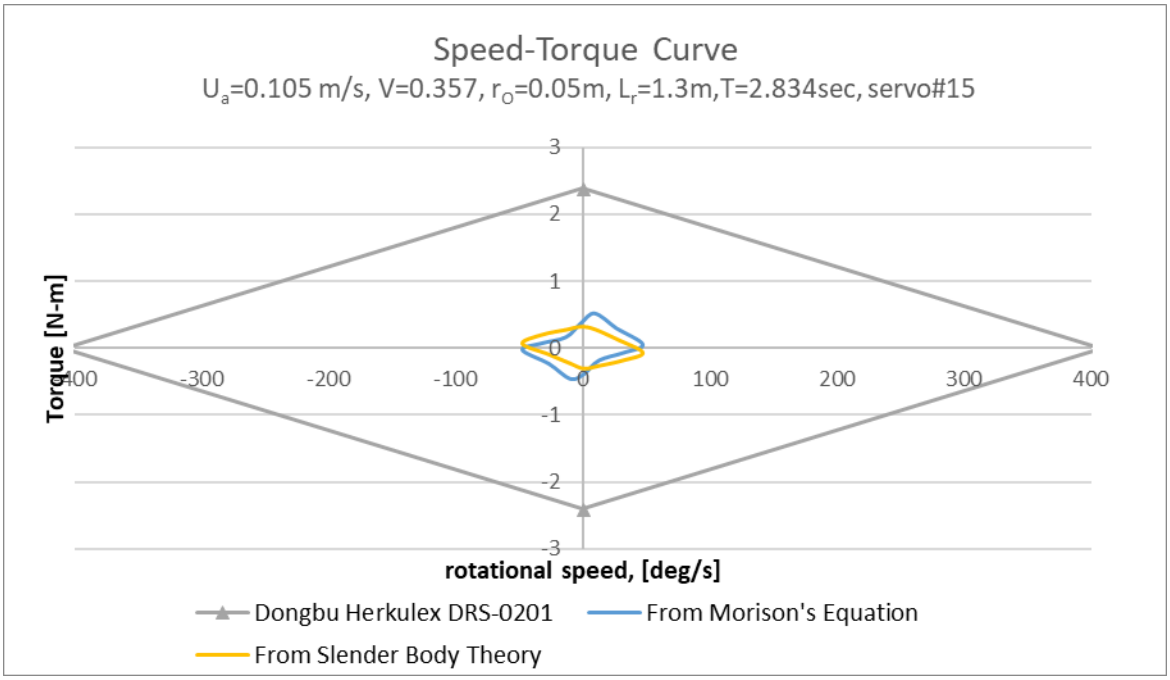
Speed-Torque Curve
U_a=0.105 m/s, V=0.357, r_O=0.05m, L_r=1.3m,T=2.834sec, servo#15
Torque [N-m]
rotational speed, [deg/s]
Dongbu Herkulex DRS-0201
From Morison's Equation
From Slender Body Theory

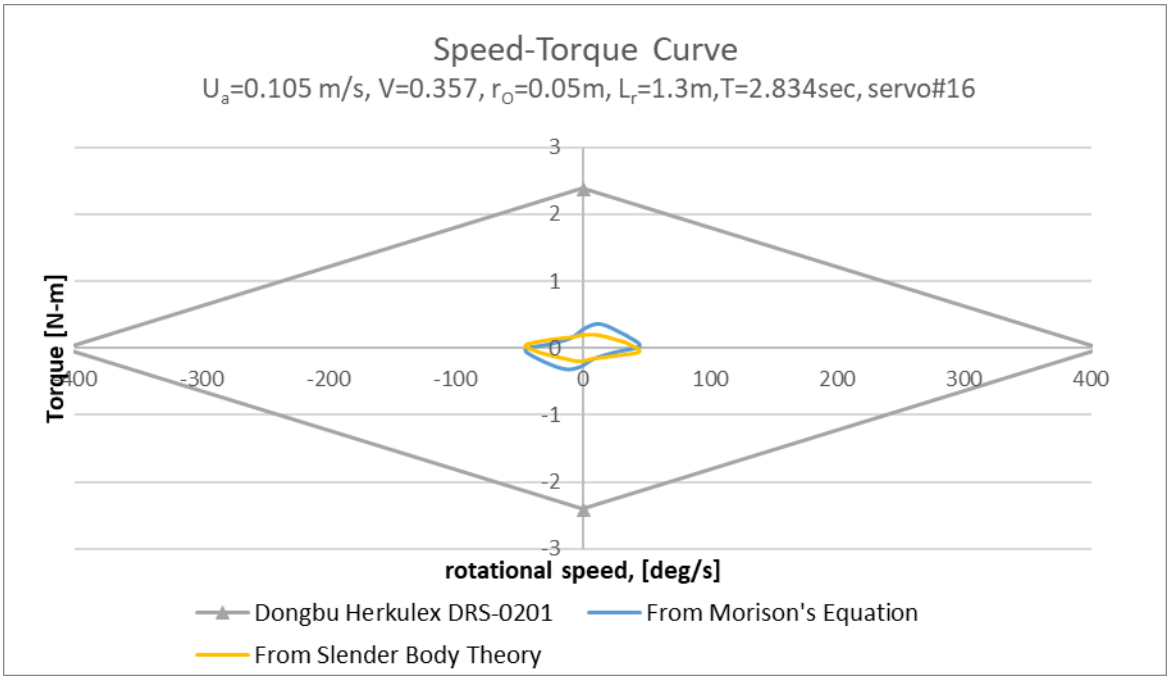
Speed-Torque Curve
U_a=0.105 m/s, V=0.357, r_O=0.05m, L_r=1.3m,T=2.834sec, servo#16
Torque [N-m]
rotational speed, [deg/s]
Dongbu Herkulex DRS-0201
From Morison's Equation
From Slender Body Theory

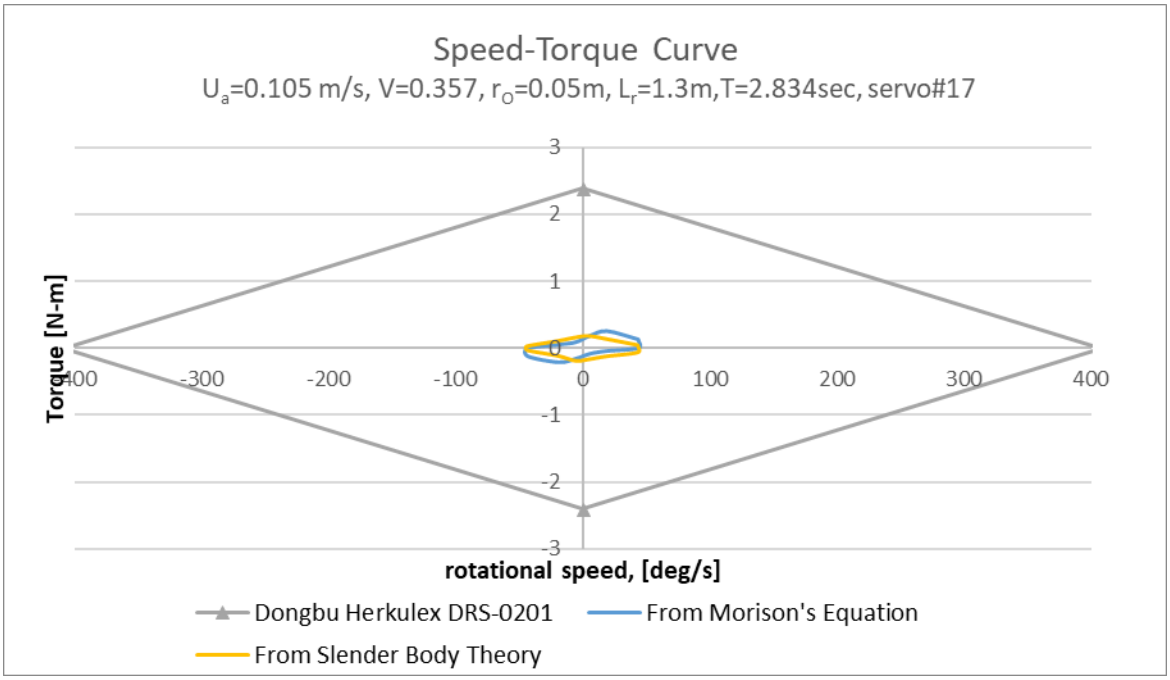
Speed-Torque Curve
U_a=0.105 m/s, V=0.357, r_O=0.05m, L_r=1.3m,T=2.834sec, servo#17
Torque [N-m]
rotational speed, [deg/s]
Dongbu Herkulex DRS-0201
From Morison's Equation
From Slender Body Theory

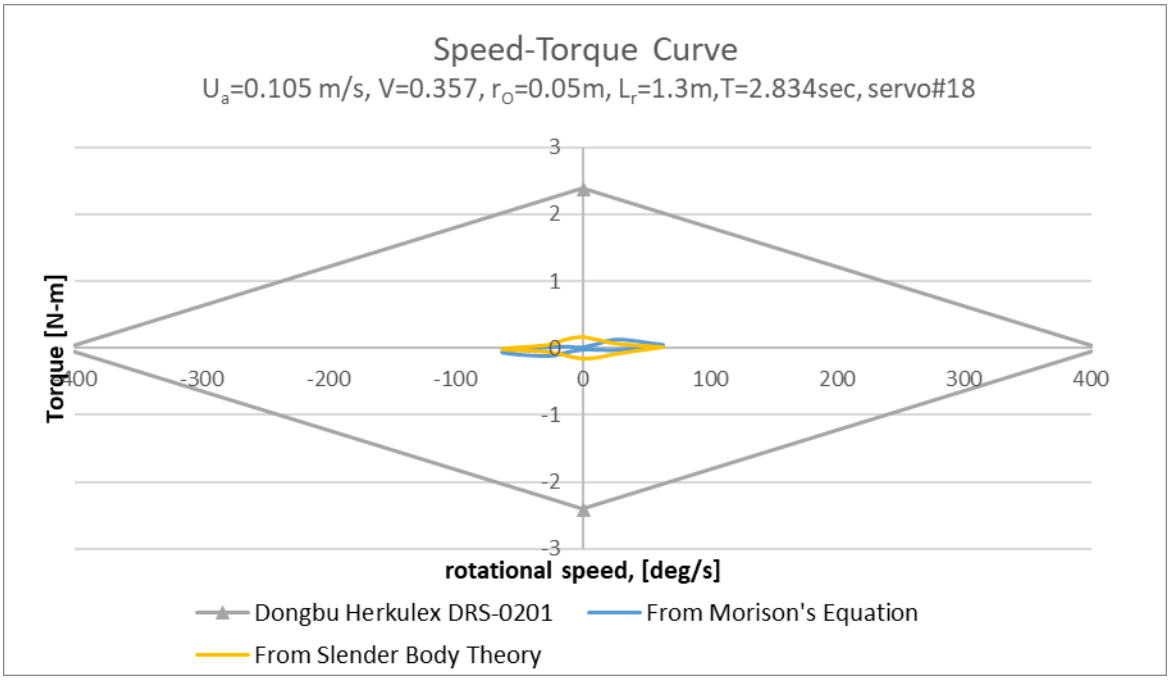
Speed-Torque Curve
U_a=0.105 m/s, V=0.357, r_O=0.05m, L_r=1.3m,T=2.834sec, servo#18
Torque [N-m]
rotational speed, [deg/s]
Dongbu Herkulex DRS-0201
From Morison's Equation
From Slender Body Theory

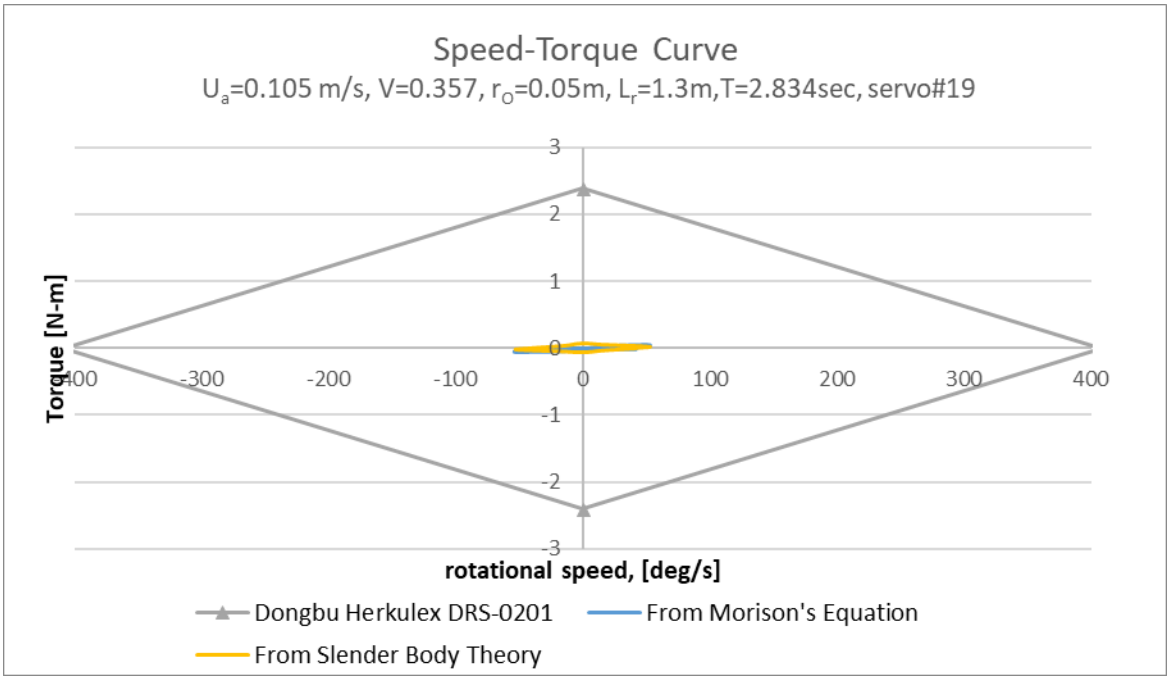
Speed-Torque Curve
Ua=0.105 m/s, V=0.357, rO=0.05m, Lr=1.3m,T=2.834sec, servo#19
Torque [N-m]
3
2
1
0
-1
-2
-3
-400
-300
-200
-100
0
100
200
300
400
rotational speed, [deg/s]
Dongbu Herkulex DRS-0201
From Morison's Equation
From Slender Body Theory

Vita

Naga Sasi Devarakonda was born in Shimla, India. She obtained her bachelor's degree in Naval Architecture and Marine Engineering from Andhra University, India in 2016. She joined the University of New Orleans in a graduate program to pursue Master of Sciences in Naval Architecture and Marine Engineering. She has successfully completed her thesis which partially fulfills the degree requirements under Dr. Brandon Michael Taravella in 2018.